

August 1985

NASA-CR-174957
19850025227

CR-174957

Contract NAS3-23940

ELEVATED TEMPERATURE CRACK GROWTH

ANNUAL REPORT

Prepared By

J.F. Yau
S.N. Malik
K.S. Kim
R.H. VanStone
J.H. Laflen

Approved By

M.L. Roberts, Technical Manager
J.A. McKenzie, Program Manager

Prepared for

National Aeronautics and Space Administration
Lewis Research Center
21000 Brookpark Road
Cleveland, Ohio 44135

GENERAL  **ELECTRIC**

Aircraft Engine Business Group
Advanced Technology Programs Dept.
Cincinnati, Ohio 45215

NASA



NF01226



August 1985

CR-174957

Contract NAS3-23940

ELEVATED TEMPERATURE CRACK GROWTH

ANNUAL REPORT

Prepared By

J.F. Yau

S.N. Malik

K.S. Kim

R.H. VanStone

J.H. Laflen

Approved By

M.L. Roberts, Technical Manager

J.A. McKenzie, Program Manager

Prepared for

National Aeronautics and Space Administration

Lewis Research Center

21000 Brookpark Road

Cleveland, Ohio 44135

GENERAL  ELECTRIC

Aircraft Engine Business Group
Advanced Technology Programs Dept.
Cincinnati, Ohio 45215

NASA

N85-33540 #

TABLE OF CONTENTS

<u>Section</u>		<u>Page</u>
1.0	INTRODUCTION	1
2.0	REVIEW OF PATH-INDEPENDENT INTEGRALS	2
3.0	NUMERICAL IMPLEMENTATION OF PATH-INDEPENDENT INTEGRALS	7
3.1	P-I Integral Computational Algorithm	7
3.2	Computation of P-I Integrals	8
3.3	Mesh Generator Program Development	32
4.0	EXPERIMENTAL WORK	35
4.1	Analog Material	35
4.2	Test Matrix	36
4.3	Task III - Analog Material (Constitutive Properties)	36
4.4	Task VII - Isothermal and TMF Crack Propagation, Analog Material	40
4.4.1	Specimen Design	40
4.4.2	Displacement Control and Measurement	47
4.4.3	Test Plan	51
4.5	Task VIII - Crack Propagation With Thermal Gradient, Analog Material	53
5.0	COMPUTER SIMULATION OF SEN SPECIMENS	54
6.0	DISCUSSION	61
7.0	REFERENCES	62

LIST OF ILLUSTRATIONS

<u>Figure</u>		<u>Page</u>
1.	Integration Paths and Area.	5
2.	Flow Chart of Postprocessor for Path-Independent Integrals Computation.	8
3.	Geometry of an ASTM Standard Compact Tension Specimen and Its Finite-Element Analysis Model.	11
4.	Near Crack-Tip Mesh Refinement and Circular Integration Paths for the Compact Tension Specimen.	12
5.	Stress-Strain Response of the Material for CYANIDE Inelastic Analysis of Compact Tension Specimen.	13
6.	Path-Independence of J-Integral Along Various Paths for Each Load Step.	15
7.	Comparison of Computed J-Integral Values with EPFM Handbook Solution.	16
8.	Blackburn J^* -Integral and Its Line and Area Integral Contributions Along Various Integration Paths for an Applied Load (P/P_o) of 1 in Compact Tension Specimen.	18
9.	Blackburn J^* -Integral for the Four Load Steps for the Compact Tension Specimen.	19
10.	Kishimoto \hat{J} -Integral and Its Line and Area Integral Contributions Along Various Integration Paths for an Applied Load (P/P_o) of 1 in Compact Tension Specimen.	20
11.	Comparison of Area and Line Integral Terms Contributions to Blackburn (J^*) and Kishimoto (\hat{J}) Integrals.	21
12.	Kishimoto \hat{J} -Integral for the Four Load Steps for the Compact Tension Specimen.	23
13.	Load Versus Load Point Displacement for the Compact Tension Specimen at Various Load Steps.	24
14.	Atluri ΔT^* Incremental Integral Along Various Integration Paths for ^P Loading and Unloading Steps on Compact Tension Specimen.	25
15.	Atluri T^* -Integral ($=\sum \Delta T^*$) Along Various Integration Paths for Loading and Unloading ^P Steps.	26

LIST OF ILLUSTRATIONS (Continued)

<u>Figure</u>		<u>Page</u>
16.	Atluri ΔT_P Incremental Integral Along Various Integration Paths for Loading and Unloading Steps on Compact Tension Specimen.	27
17.	Atluri T_P -Integral ($=\Sigma \Delta T_P$) Along Various Integration Paths for Loading and Unloading Steps.	28
18.	Comparison of Present Results for Atluri T_P and T^* Integrals as a Function of Applied Loading and Unloading Steps in Compact Tension Specimen.	29
19.	Atluri Integrals T_P and T^* for Loading and Unloading Steps in a Compact Tension Specimen Reported in Reference 14.	30
20.	Comparison of Various P-I Integrals Obtained in Present Study for Loading Steps on Compact Tension Specimen.	31
21.	An Example of Square Mesh Generated for a Single Edge Crack Specimen.	33
22.	An Example of Fan Mesh Generated for a Single Edge Crack Specimen.	34
23.	Specimen Bar Smooth Tensile, Rupture or Creep Rupture, 0.250 Gage Diameter.	38
24.	Specimen Bar Cylindrical LCF.	39
25.	Variation of Plastic Strain Range with Total Strain Range for Alloy 718 at 1000° F with $A_\epsilon = \infty$.	42
26.	Buttonhead Single Edge Notch (SEN) Specimen.	43
27.	Examples of Hysteresis Loops in SEN Propagation Tests.	45
28.	Examples of Alloy Hysteresis Loops in Cyclic Test (1200° F), $A = \infty$, 0.017 Strain Range, 2.0×10^{-4} Strain Rate.	46
29.	Variation of Maximum and Minimum Stress in Alloy 718 SEN and Cyclic Test.	48
30.	Schematic Drawing of SEN Test Method.	50
31.	Buttonhead Specimen Three-Dimensional Finite-Element Model.	55

LIST OF ILLUSTRATIONS (Concluded)

<u>Figure</u>		<u>Page</u>
32.	Top View and Elevation of the SEN Buttonhead Specimen Three-Dimensional Finite-Element Model.	56
33.	Normal Displacement Variation in Gage Section for Three-Dimensional Elastic Analysis of Specimen Subjected to Constant Axial Displacement at Buttonhead.	57
34.	Normal Stress Variation in Gage Section for Three-Dimensional Elastic Analysis of Specimen Subjected to Constant Axial Displacement at Buttonhead.	58
35.	Lateral Displacement Profile of the Buttonhead Single Edge Crack Specimen Subjected to Uniform Axial Displacement (Dotted Lines Show Undeformed Shape).	60

LIST OF TABLES

<u>Table</u>		<u>Page</u>
I.	Summary of P-I Integrals.	3
II.	Comparison of Computed J-Integral Values with EPFM Handbook Solution.	17
III.	Variation of Alloy 718 Elastic Modulus and Creep Properties with Temperature.	36
IV.	Composition of Alloy 718 Plate.	37
V.	Task III Test Matrix.	41
VI.	Summary of Estimated Values of J, δ , and δ_t for Alloy 718 at 1200° F.	49
VII.	Task VII Test Matrix.	52
VIII.	Variation of Cycle Period and Cycle Accumulation in Strain-Rate-Controlled Tests with Strain Rate and Range.	53

1.0 INTRODUCTION

Critical gas turbine engine hot section components such as blades, vanes, and combustor liners tend to develop minute cracks during the early stages of operation. Under conditions of fatigue and creep, these cracks may grow to critical size. Current methods of predicting growth rates or critical crack sizes are inadequate, leaving two extreme courses of action. The first is to take an optimistic view with the attendant risk of an excessive number of service failures. The second is to take a pessimistic view and accept an excessive number of rejections-for-cause at considerable expense in parts and downtime. Clearly, it is imperative to develop reliable methods of predicting crack growth rates and critical crack sizes.

To develop such methods, it is necessary to relate the processes that control crack growth in the immediate vicinity of the crack tip to parameters that can be calculated from remote quantities such as forces, stresses, or displacements. The most likely parameters appear to be certain path-independent (P-I) contour integrals; several have already been proposed for application to high-temperature inelastic problems. A thorough analytical and experimental evaluation of these parameters needs to be made and would include elevated-temperature isothermal and thermomechanical fatigue, both with and without thermal gradients.

In any investigation of fatigue crack growth, the problem of crack closure must be addressed in order to develop the appropriate crack growth model. Analytically, this requires the use of gap elements in a nonlinear finite-element code to predict closure loads. Such predictions must be verified experimentally through detailed measurements. The best method for measuring crack closure has not been established in previous studies.

It is the purpose of this program to define the capability of currently available P-I integrals to correlate fatigue crack propagation under conditions that simulate the turbojet engine combustor liner environment. In addition, the utility of advanced fracture mechanics measurements will be evaluated and determined during the course of the program. These goals will be accomplished by means of a 2-year, nine-task, combined experimental and analytical program. Initially, a specimen design and crack displacement measurement method will be decided. An analog material was selected based on its ability to simulate high temperature behavior at lower temperatures in order to facilitate experimental measurements. Available P-I integrals were reviewed; the best approaches were selected for evaluation with experimental data. The experimental data will include cyclic crack growth tests under thermomechanical conditions and under thermal gradients.

This report presents the progress made during the first year of the contract.

2.0 REVIEW OF PATH-INDEPENDENT INTEGRALS

As a parameter for predicting crack growth in the elastic-plastic regime, the utility of the J-integral is limited. The theoretical basis of the J-integral does not allow the extension of its usage to nonproportional loading and unloading in the plastic regime, nor can it be used in the presence of a temperature gradient and material inhomogeneity. A typical example where all these limiting factors are operative would be the hot section components of a gas turbine in mission cycles.

In recent years there has been considerable effort to modify or reformulate the path-independent (P-I) integral. Consequently, a number of new P-I integrals have emerged. These include the J^* , \hat{J} , J_θ , ΔT_p , ΔT^* integrals and two thermoelastic integrals, J_w and J_G . These P-I integrals have been critically reviewed in this program. In this report, only a brief synopsis of the review is presented. In Reference 1, a detailed discussion of the available P-I integrals is given as a result of the review performed on the present contract. The theoretical background has been examined with particular attention to whether or not the path-independence is maintained in the presence of (1) nonproportional loading, (2) unloading in the plastic regime, and (3) a temperature gradient and material inhomogeneity. The relation among the P-I integrals, salient features, and limitations was investigated. The physical meaning, the possibility of experimental measurement, and the computational ease were also examined. The summary of the review is presented in Table I. In view of the requirements associated with performing the forthcoming tasks in this program, the following conclusions were made:

1. The J^* , \hat{J} , ΔT_p , and ΔT^* integrals maintain path-independence under the thermomechanical cycles that will be used in tests during this program and will be simulated numerically in subsequent tasks. Although the physical meaning of these P-I integrals needs to be pursued further, they represent the logical choices for continued evaluation in this program.
2. The J , J_w , J_G , and J_θ integrals have limited capabilities. The J_w and J_G integrals are usable only for thermoelastic programs with homogeneous material properties. These integrals may be helpful in predicting crack growth in a small temperature gradient field and under small-scale yielding conditions. The J_θ integral is a modified version of J (modified to include the thermal strain). Thus, it cannot be used with substantially nonproportional loading and unloading in the plastic regime. However, it would be worthwhile to investigate the utility of operationally defined J and possibly J_θ for the test cycles in this program.

Table I. Summary of P-I Integrals.

P-I Integral	Measure of Crack Tip Severity	Physical Meaning (5)			Capability to Handle				Computation (Integrals involved)	Experimental ⁽¹⁾ Measurement
		Elastic	Thermo-elastic	Plastic	Proport'l loading (plastic regime)	Nonproport'l & Loading/Unloading	Thermal Strain	Material Inhomogeneity		
J	Yes	$-\frac{\partial P}{\partial a}$	---	$-\frac{\partial P}{\partial a}$	Yes	No	No	No	Line	Yes
J _w	Yes	$-\frac{\partial P}{\partial a}$	$-\frac{\partial \phi}{\partial a}$	---	No	No	Yes	No	Line +Area	Yes
J _G	Yes	$-\frac{\partial P}{\partial a}$	$-\frac{\partial \phi}{\partial a}$	---	No	No	Yes	No	Line	Yes
J _θ	Yes	$-\frac{\partial P}{\partial a}$	$-\frac{\partial \phi}{\partial a}$	$-\frac{\partial P}{\partial a}$ (2)	Yes	No	Yes	No	Line +Area	Yes
J*	Yes	$-\frac{\partial P}{\partial a}$	$-\frac{\partial \phi}{\partial a}$	Unknown	Yes	Yes	Yes	Yes	Line +Area	No (6)
\hat{J}	Yes	Rate of work done to crack tip by surrounding Material (3)			Yes	Yes	Yes	Yes	Line +Area	No
ΔT_P^*	Yes	$-\frac{\Delta \pi}{da}$ for proport'l loading ⁽⁴⁾			Yes	Yes	Yes	Yes	Line +Area	No ⁽⁷⁾
ΔT_P	No ⁽⁷⁾	$-\frac{\Delta \pi}{da}$ for proport'l loading ⁽⁴⁾			Yes	Yes	Yes	Yes	Line +Area	Yes

NOTE: (1) Yes if it can be expressed as the rate of a potential, or if it has only line integrals, and the area integrals are negligible

(2) $-\frac{\partial \phi}{\partial a}$ for thermoplastic proportional loading

(3) With the assumption of a rigid fracture process zone at the crack tip independent of crack size

(4) Further study is needed for the case of thermomechanical loading

(5) P = Potential energy, ϕ = Global thermodynamic potential, $\Delta \pi$ = Incremental potential

(6) Limited computational results have significant line integral contributions

(7) Yes for Proportional Loading at local (crack-tip) and global level

The P-I integrals reviewed in this program are shown here. The index notation was used. The common variables are: σ_{ij} = stress tensor, ϵ_{ij} = strain tensor, u_i = displacement vector, t_i = traction vector, θ = relative temperature, α = thermal expansion coefficient, μ and λ = Lamé's constants. Refer to Figure 1 for integration paths and areas.

Rice's J-Integral (Reference 2)

$$J = \int_{\Gamma} (n_1 W - t_i u_{i,1}) ds$$

$$\text{where } W = \int_0^{\epsilon_{ij}} \sigma_{ij} d\epsilon_{ij}$$

Wilson and Yu's Thermoelastic Integral (Reference 3)

$$J_W = \int_{\Gamma} (n_1 W - t_i u_{i,1}) ds - \alpha(3\lambda + 2\mu) \int_A [\frac{1}{2}(\theta \epsilon_{ii})_{,1} - \epsilon_{ii} \theta_{,1}] dA$$

Where

$$W = \frac{1}{2} \sigma_{ij} \epsilon_{ij}$$

Gurtin's Thermoelastic Integral (Reference 4)

$$J_G = \int \left[n_1 W - t_k u_{k,1} - \frac{\alpha^2 (3\lambda + 2\mu)^2}{2(\lambda + \mu)} \theta^2 n_1 + \frac{\alpha \mu (3\lambda + 2\mu)}{(\lambda + \mu)} \left(\theta \frac{\partial u_1}{\partial n} - u_1 \frac{\partial \theta}{\partial n} \right) \right] ds$$

Where

$$\frac{\partial}{\partial n} = n_j \frac{\partial}{\partial x_j}$$

and

$$W = \mu \epsilon_{ij} \epsilon_{ij} + \frac{\lambda}{2} (\epsilon_{kk})^2$$

The J_{θ} -Integral by Ainsworth et al. (Reference 5)

$$J_{\theta} = \int_{\Gamma} (n_1 W - t_i u_{i,1}) ds + \int_A \sigma_{ij} \epsilon_{ij,1} dA$$

where

$$W(\epsilon'_{ij}) = \int_0^{\epsilon'_{ij}} \sigma_{ij} d\sigma'_{ij}, \text{ and } \epsilon'_{ij} = \epsilon_{ij} - \epsilon_{ij}^{\theta}$$

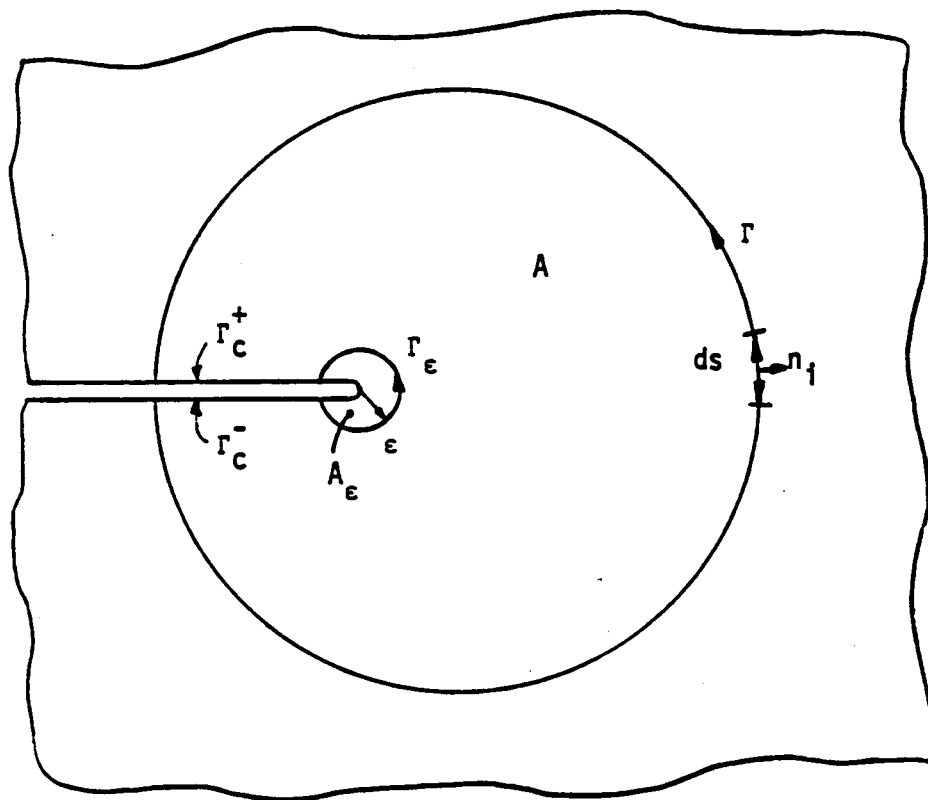


Figure 1. Integration Paths and Areas.

The J^* - Integral by Blackburn (References 6, 7)

$$J^* = \int_{\Gamma + \Gamma_c} (\frac{1}{2} \sigma_{ij} u_{i,j} dx_2 - t_i u_{i,1} ds) + \int_A (\frac{1}{2} \sigma_{ij} u_{i,j,1} - \frac{1}{2} \sigma_{ij,1} u_{ij}) dA$$

The \hat{J} -Integral by Kishimoto, Aoki, and Sakata (Reference 8)

$$\hat{J} = - \int_{\Gamma + \Gamma_c} t_i u_{i,1} ds + \int_A \sigma_{ij} \varepsilon_{ij,1} dA$$

The ΔT - Integrals by Atluri et al (Reference 9)

$$\Delta T_p^* = \int_{\Gamma + \Gamma_c} | n_i \Delta W - (t_i + \Delta t_i) \Delta u_{i,1} - \Delta t_i u_{i,1} | ds \\ + \int_A | \Delta \sigma_{ij} (\varepsilon_{ij,1} + \frac{1}{2} \Delta \varepsilon_{ij,1}) - \Delta \varepsilon_{ij} (\sigma_{ij,1} + \frac{1}{2} \Delta \sigma_{ij,1}) | dA$$

$$\Delta T_p = \int_{\Gamma + \Gamma_c} | n_i \Delta W - (t_i + \Delta t_i) \Delta u_{i,1} - \Delta t_i u_{i,1} | ds \\ + \int_{A_s - A_\Gamma} | (\sigma_{ij,1} + \frac{1}{2} \Delta \sigma_{ij,1}) \Delta \varepsilon_{ij} - (\varepsilon_{ij,1} + \frac{1}{2} \Delta \varepsilon_{ij,1}) \Delta \sigma_{ij} | dA$$

where

$$\Delta W = (\sigma_{ij} + \frac{1}{2} \Delta \sigma_{ij}) \Delta y_{i,j}$$

and A_s is the total area and A_Γ is the area in Γ .

3.0 NUMERICAL IMPLEMENTATION OF P-I INTEGRALS

As part of the contract, General Electric developed a finite-element postprocessor for calculating the path-independent (P-I) integrals which will be evaluated in detail later in the contract. This section discusses the computational algorithms used in the postprocessor and gives some numerical results for one crack geometry.

3.1 P-I INTEGRAL COMPUTATIONAL ALGORITHM

Computational algorithms have been developed for numerically implementing various P-I fracture mechanics integrals under consideration in the current work. These postprocessor numerical algorithms assume that an accurate inelastic solution is available by using a finite-element model of a specimen geometry containing a crack. In the present work, the two-dimensional (2D) finite-element computer code CYANIDE, which is a General Electric program, is used for inelastic stress analysis. The CYANIDE program uses the incremental theory of plasticity and accounts for both time-independent plastic flow (plasticity) and time-dependent plastic flow (creep). It uses linearly varying displacements in each triangular element subdivision of a model, resulting in constant strains over each element.

A flow chart of the postprocessor P-I integrals computational program is shown in Figure 2. The output files from the CYANIDE solution for element stresses and strains, nodal displacements, nodal coordinates, and nodal connectivity for each element are read and stored by the postprocessor program. Paths of integration surrounding the crack tip are chosen so that they consist of sides of the triangular elements. An option for user-specified or automatic selection of node numbers is available for defining the integration paths. For the automatic search option, the program selects a set of nodes that keep a fairly constant radial distance from the crack tip, thereby generating an approximate circular integration path. For each line segment along the integration path, the unit normal vector and its Cartesian components are computed. The quantities, such as σ_{ij} , W , and $U_{i,j}$, that appear in the integrand of P-I integrals are interpolated at the midpoint of the path segment by taking weighted averages of those for the elements containing the segment. For example, an interpolated quantity F at the midpoint of a line segment is given as:

$$F = F_1 \left(\frac{d_2}{d_1 + d_2} \right) + F_2 \left(\frac{d_1}{d_1 + d_2} \right)$$

where F_1 and F_2 are the values for the two elements connected to the path segment, and d_1 and d_2 are the respective distances of those element centroids from the midpoint of the path segment.

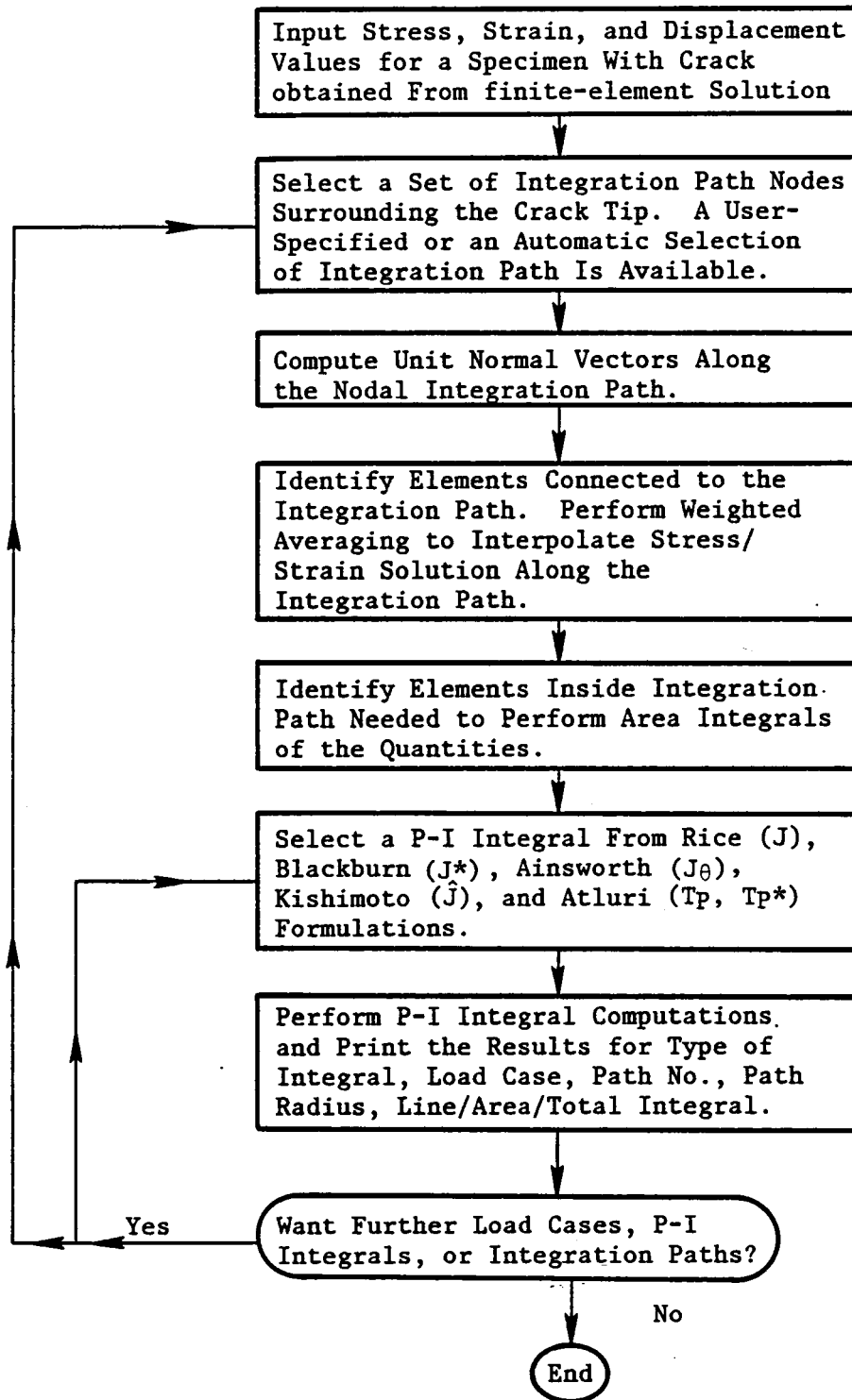


Figure 2. Flow Chart of Postprocessor for Path-Independent Integrals Computation.

The displacement derivatives for an element are accurately computed from displacement components and coordinates of its vertices (nodes) by using the equations gotten from the shape functions. The shape functions for linear variation of displacements in a triangular element are given by

$$u(x,y) = (a_0 + a_1x + a_2y)$$

$$v(x,y) = (b_0 + b_1x + b_2y)$$

The displacement derivatives for the element are shown to be

$$\frac{\partial u}{\partial x} = \frac{u_1(y_2 - y_3) + u_2(y_3 - y_1) + u_3(y_1 - y_2)}{x_1x_2 + x_2y_3 + x_3y_1 - x_2y_1 - x_3y_2 - x_1y_3}$$

and

$$\frac{\partial v}{\partial x} = \frac{v_1(y_2 - y_3) + v_2(y_3 - y_1) + v_3(y_1 - y_2)}{x_1x_2 + x_2y_3 + x_3y_1 - x_2y_1 - x_3y_2 - x_1y_3}$$

where the subscripts 1, 2, and 3 represent nodal values at the element vertices. Similar relationships are obtained for derivatives of element stresses.

Elements inside an integration path are identified by establishing a list of nodes that are either inside or along the integration path, then searching from the global element-node connectivity table to find only those elements for which each and every vertex node is either inside or along the integration contour. In this process, a counter keeps track of the total number of elements found for computing area integrals and the total surface area inside the given contour.

Once the integration path and the elements inside a path of a given size are selected, the user is given the option of choosing any one of the P-I integrals from a list. At present, the list includes formulations of Rice (J), Blackburn (J*), Ainsworth (J_θ), Kishimoto (Ĵ), and Atluri (Tp and Tp*) P-I integrals. Other P-I integrals, such as Wilson and Yu (J_w), Gurtin (J_G), Miyamoto (J, Reference 10; J_{3D}, References 11, 12), could be included by adding subroutines to compute the additional terms necessary to define them. The selected P-I integral option activates the appropriate subroutines to compute line and area integral terms for the desired integration contours.

Other P-I integrals, other integration paths, and other load cases (for which a stress analysis solution is already available in CYANIDE output files) can also be computed. The various computed values can then be printed or

graphically plotted. Currently, the following options for plotting the results are available:

1. P-I integral versus distance (of various paths from the crack tip) for all load cases
2. P-I integral versus applied load on the specimen for particular integration paths
3. Comparison of various P-I integral as a function of applied load
4. Components (line, area, total) of P-I integral versus distance of integration paths (from the crack tip)
5. Components (line, area, total) of P-I integrals versus applied load.

Similarly, the print option provides a value of P-I integrals in E-format to display the results with accuracy up to four significant digits. Improvements in user-friendliness and input data accuracy checks are being made as needed in the postprocessor program.

3.2 COMPUTATION OF P-I INTEGRALS

To test the implementing of the postprocessor computer program, the P-I integrals were computed for a compact-tension specimen. The geometry of an ASTM standard compact-tension specimen and the finite-element mesh used to model half of the specimen are shown in Figure 3. The model consists of 429 nodes and 782 triangular elements. Dimensions chosen in this study for the width b and the crack length a are 2 inches and 1 inch, respectively. The detailed mesh refinement near the crack tip is shown in Figure 4. There are 12 elements, each subtending 15° angle and joining at a single vertex point to form the crack tip. Near crack-tip mesh refinement, having radial and tangential lines emanating from the crack tip, provides much greater solution accuracy in comparison to models with a uniform distribution of elements in the crack plane.

For elastoplastic analysis, the following Ramberg-Osgood-type stress-strain behavior of material is used:

$$E = (\sigma/E) + \alpha \epsilon_0 (\sigma/\sigma_0)^n$$

with $E = 30 \times 10^6$ psi, $\alpha = 1.0$, $\epsilon_0 = 0.001$, $\sigma_0 = 30 \times 10^3$ psi, $n = 5$, and $\nu = 0.3$.

Figure 5 shows a graphical representation of this stress-strain behavior. The CYANIDE program accepts multilinear stress-strain input for elastoplastic analysis like the one shown in Figure 5.

The plane-stress state of deformation was assumed. Applied load, P , on the compact tension specimen was increased in steps so that: $P/P_0 = 0.25$, 0.5 , 0.75 , and 1.0

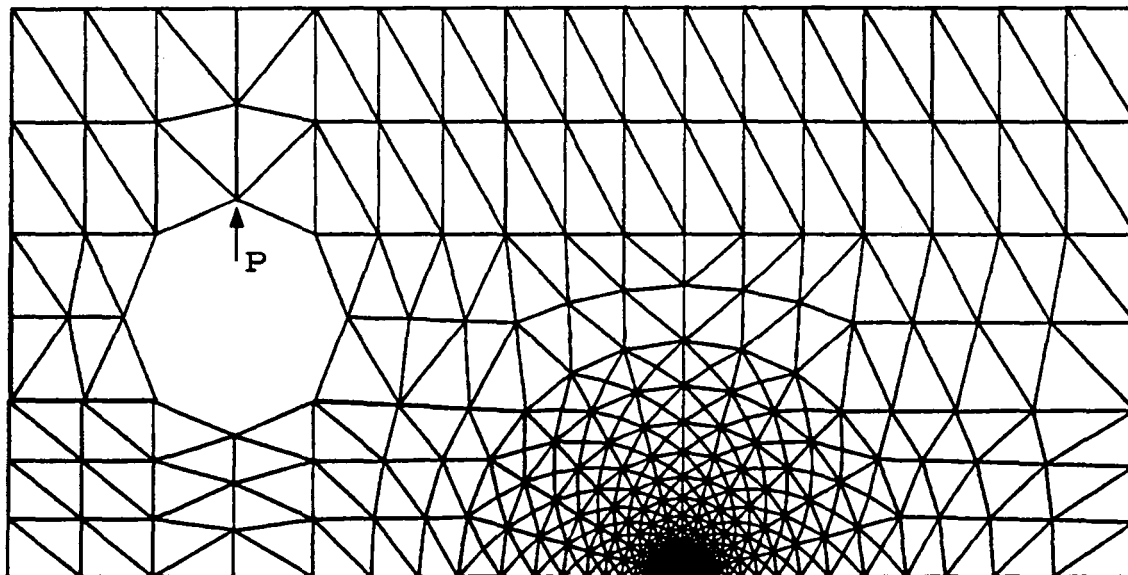
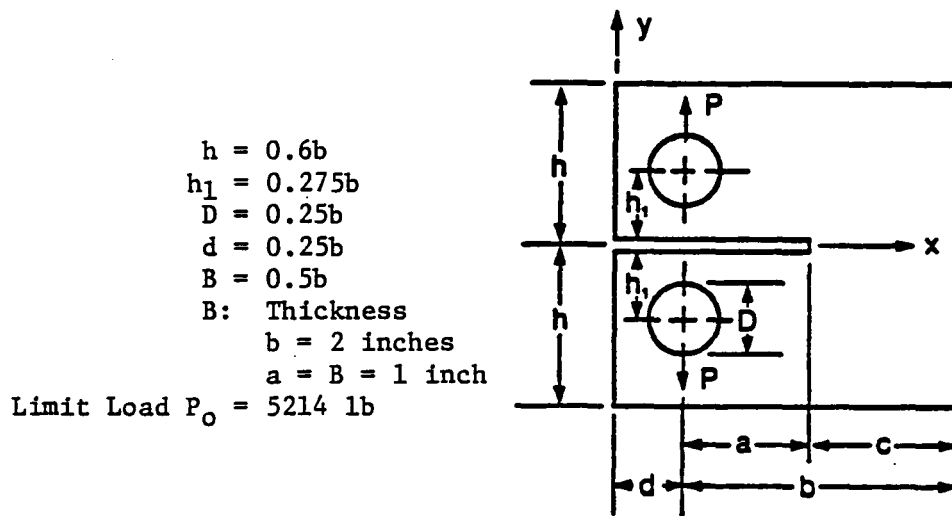


Figure 3. Geometry of an ASTM Standard Compact Tension Specimen and its Finite-Element Analysis Model.

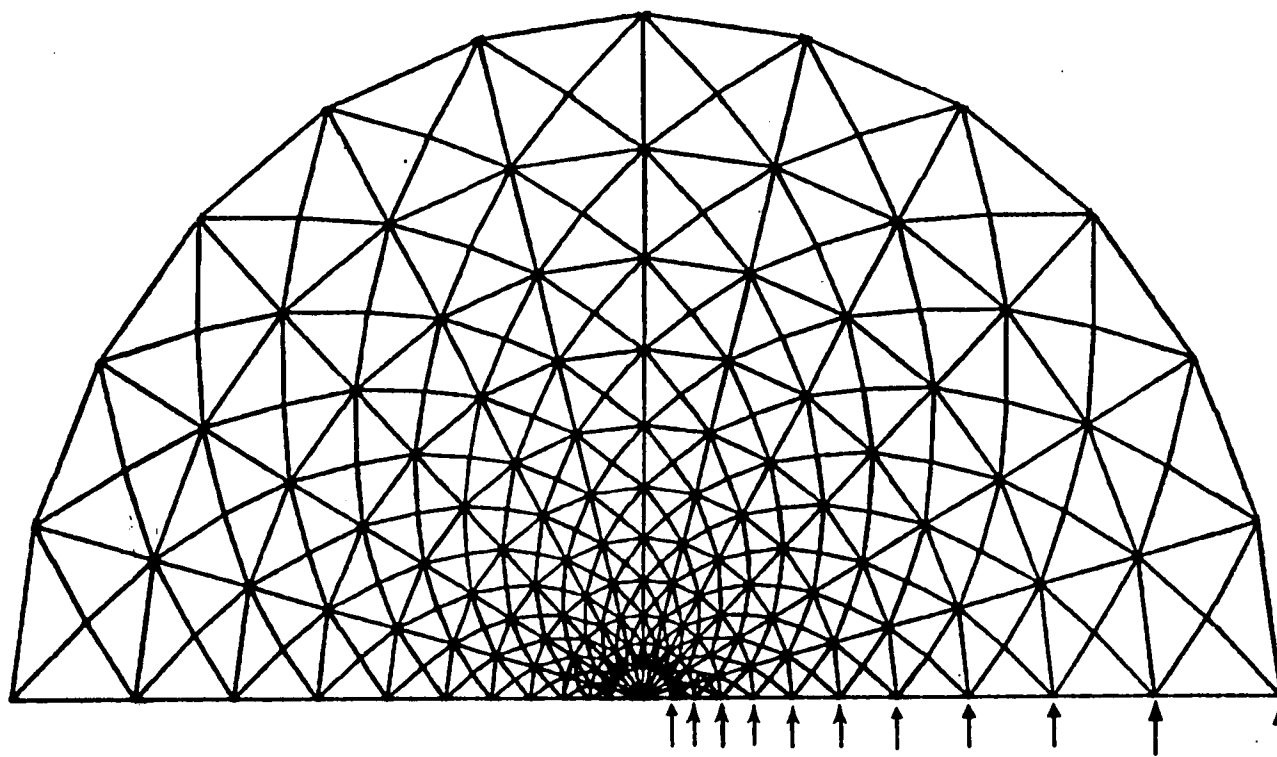


Figure 4. Near Crack-Tip Mesh Refinement and Circular Integration Paths for the Compact Tension Specimen.

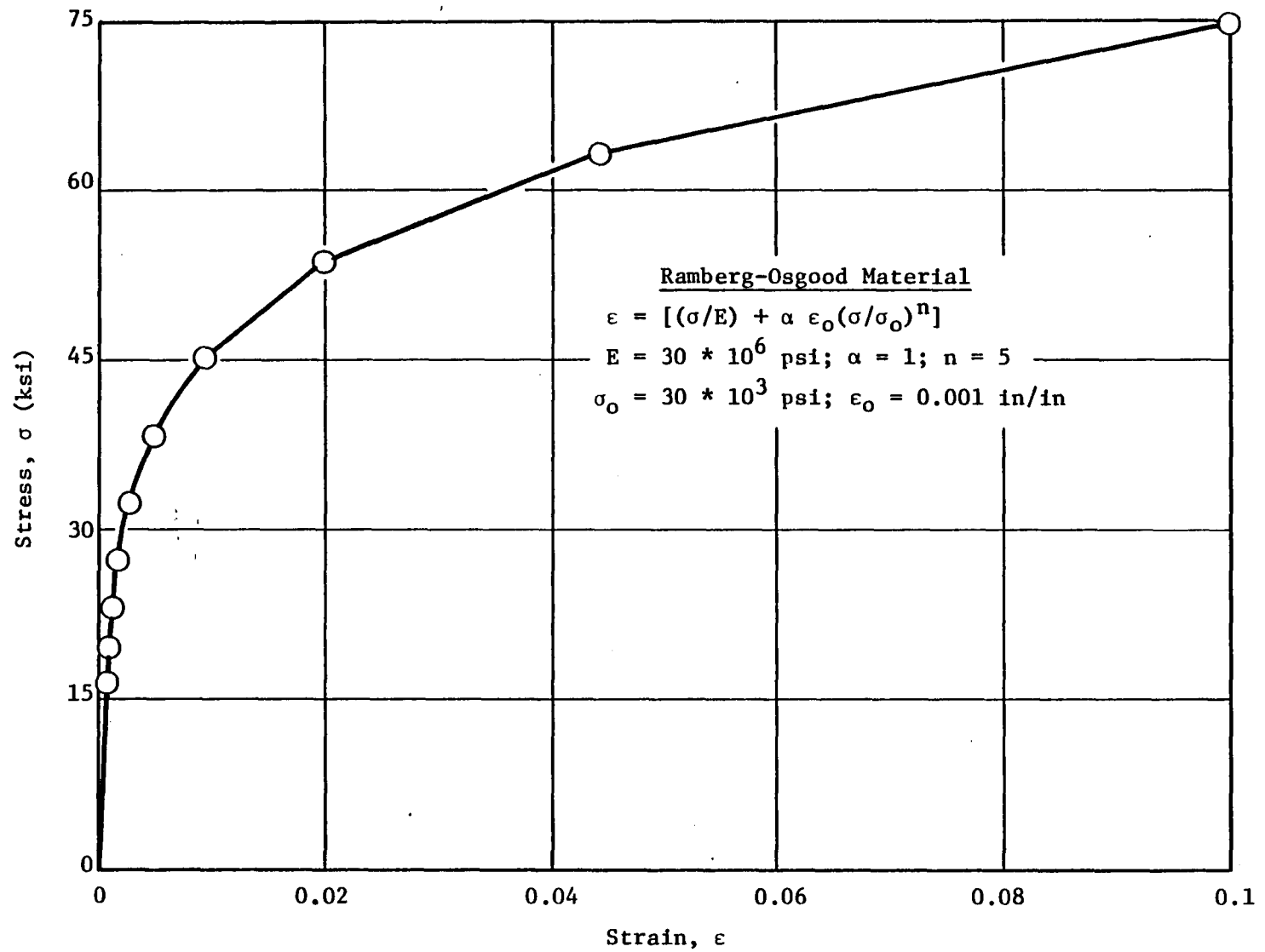


Figure 5. Stress-Strain Response of the Material for CYANIDE Inelastic Analysis of Compact Tension Specimen.

where: $P_0 = (1.071 \eta c \sigma_0)$

is the limit load per unit thickness (Reference 13), and

$$\eta = [(2a/c)^2 + 2(2a/c) + 2]^{1/2} - [(2a/c) + 1]$$

For the compact tension specimen at hand, $a = c = 1$ inch, therefore $\eta = 0.1623$ and the limit load $P_0 = 5214$ lb/inch thickness.

J-integral results for the four load steps are shown in Figure 6 for each integration path. Integration paths are circular line segments surrounding the crack tip as shown in Figure 4. It can be seen in Figure 6 that for lower values of applied load, $P/P_0 = 0.25$ and 0.5 , path-independence is preserved for all paths represented in terms of distances from the crack tip. However, for higher values of the applied load, the J-integral is path-independent for most of the paths that are slightly away from the crack tip. For paths very close to the crack tip, path-independence could be achieved by further refining the near-tip finite-element mesh to model significantly higher stress and strain gradients at larger values of the applied load.

A comparison of the computed J-integral values, averaged over all integration paths at each value of the applied load, was done with Elastoplastic Fracture Mechanics (EPFM) Handbook solutions (Reference 12) for the Ramberg-Osgood material behavior in the given compact tension specimen. Figure 7 shows a comparison of the present J-integral results with an estimation scheme solution from the EPFM Handbook. It can be seen that the comparison is excellent except at the highest value of applied load, for which the difference in J-integral values is 8%. This comparison is also shown in tabular form in Table II. Note that the EPFM Handbook solutions employ effective crack lengths, a_{eff} , which are based on Irwin's plastic zone correction factors modified for strain-hardening (Reference 13). For example, the handbook solutions have a_{eff} values of 1.003, 1.014, 1.031, and 1.055 inches, respectively, at the four load steps ($P/P_0 = 0.25, 0.5, 0.75$, and 1.0), whereas the present CYANIDE elastoplastic stress analysis solutions are for a single crack length of 1 inch.

Figure 8 shows Blackburn J^* -integral values along various integration paths at a load level, P/P_0 , of 1. The area integral contributions are small and have negative values. It can be seen that the J^* -integral is path-independent for all paths that are slightly away from the crack tip. Figure 9 shows a degree of path-independence for J^* -integral at all four load steps for the compact tension specimen. Similar to Figure 6, it is evident in Figure 9 that the path-independence is maintained to a greater degree for lower values of the applied load. Path-independence could be improved further by additional refinement of the finite element mesh used in the analysis.

The Kishimoto integral, \hat{J} , is shown along various integration paths for an applied load, P/P_0 , of 1 in Figure 10. As compared to Figure 8 for the Blackburn J^* -integral, it can be seen that the area integral contribution for the Kishimoto \hat{J} -integral is quite significant. This fact is further emphasized in Figure 11 where the averaged J^* and \hat{J} integral values (and their

Rice-J

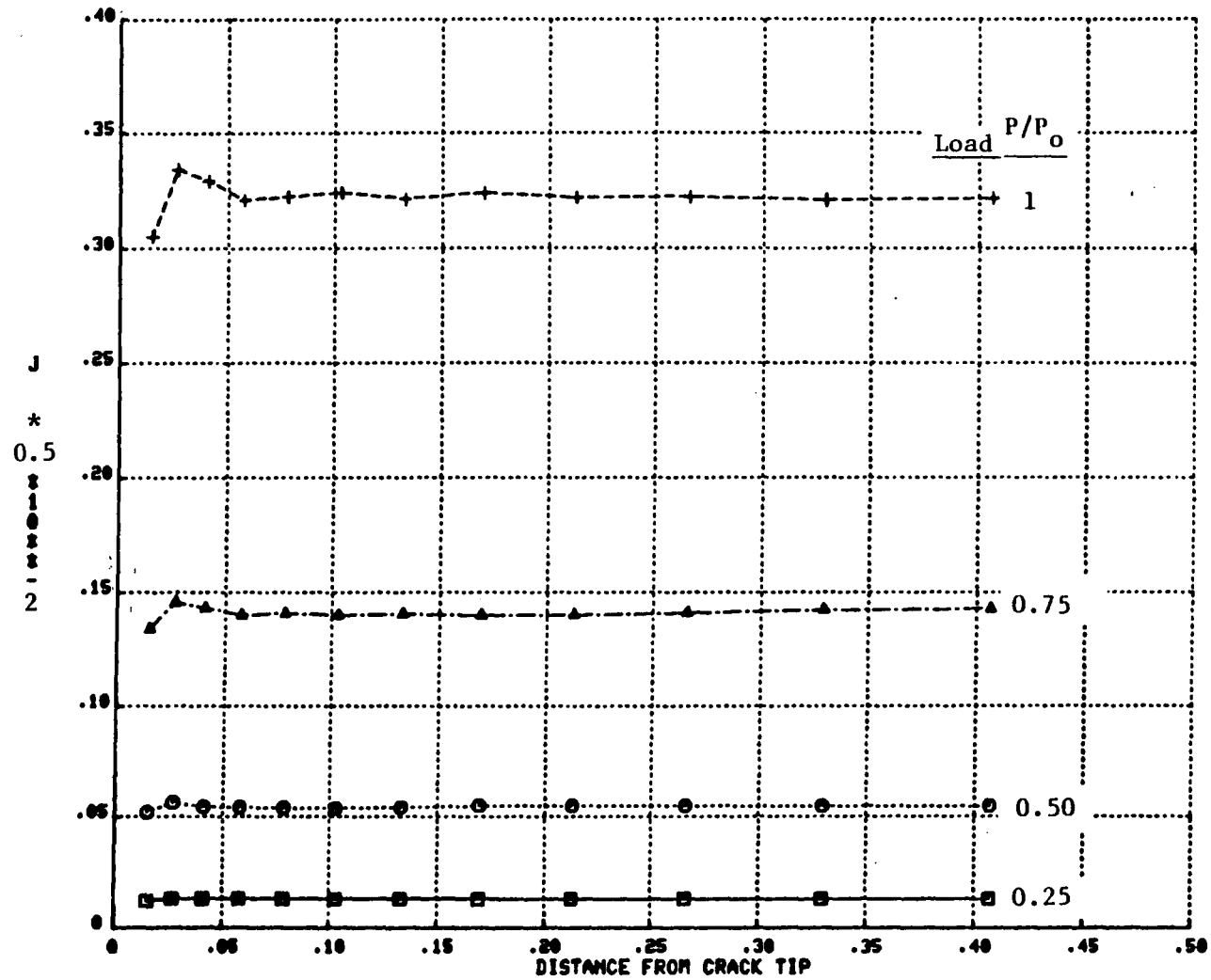


Figure 6. Path-Independence of J-Integral Along Various Paths for Each Load Step.

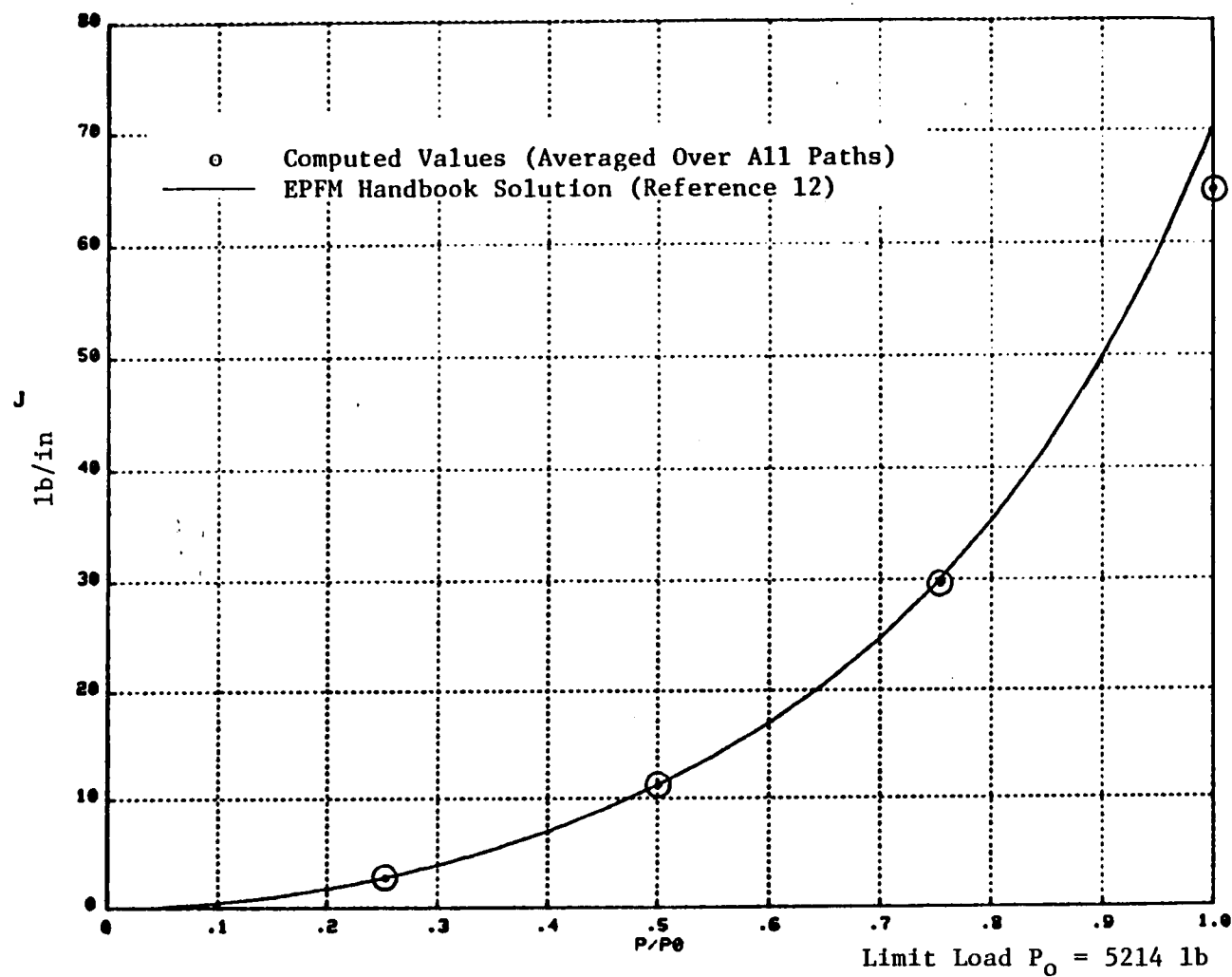


Figure 7. Comparison of Computed J-Integral Values With EPFM Handbook Solution.

Table II. Comparison of Computed J-integral Values
With EPFM Handbook Solution.

<u>Applied Load, P (lb)</u>	<u>Effective* Crack Length, a_{eff} (inch)</u>	<u>J-integral (Handbook), lb/in</u>	<u>J-integral (Present work), lb/in</u>	<u>Percent Difference</u>
260.699	1.000	0.10451		
521.398	1.001	0.41858		
782.097	1.001	0.94394		
1042.796	1.002	1.6839		
1303.495	1.003	2.6438	2.5307	4.28
1564.194	1.005	3.8323		
1824.893	1.007	5.2618		
2085.592	1.009	6.9502		
2346.291	1.011	8.9225		
2606.990	1.014	11.212	10.856	3.18
2867.689	1.017	13.865		
3128.388	1.020	16.937		
3389.088	1.023	20.502		
3649.787	1.027	24.653		
3910.486	1.031	29.503	28.147	4.6
4171.185	1.035	35.191		
4431.884	1.040	41.883		
4692.583	1.045	49.778		
4953.282	1.050	59.113		
5213.981	1.055	70.164	64.493	8.1

(*) effective crack length includes plastic zone correction factor (Reference 12)

$$a_{eff} = \left[a + \frac{1}{2\pi} \cdot \frac{(n-1)}{(n+1)} \cdot \left(\frac{K_I}{\sigma_o} \right)^2 \cdot \frac{1}{1+(P/P_o)^2} \right]$$

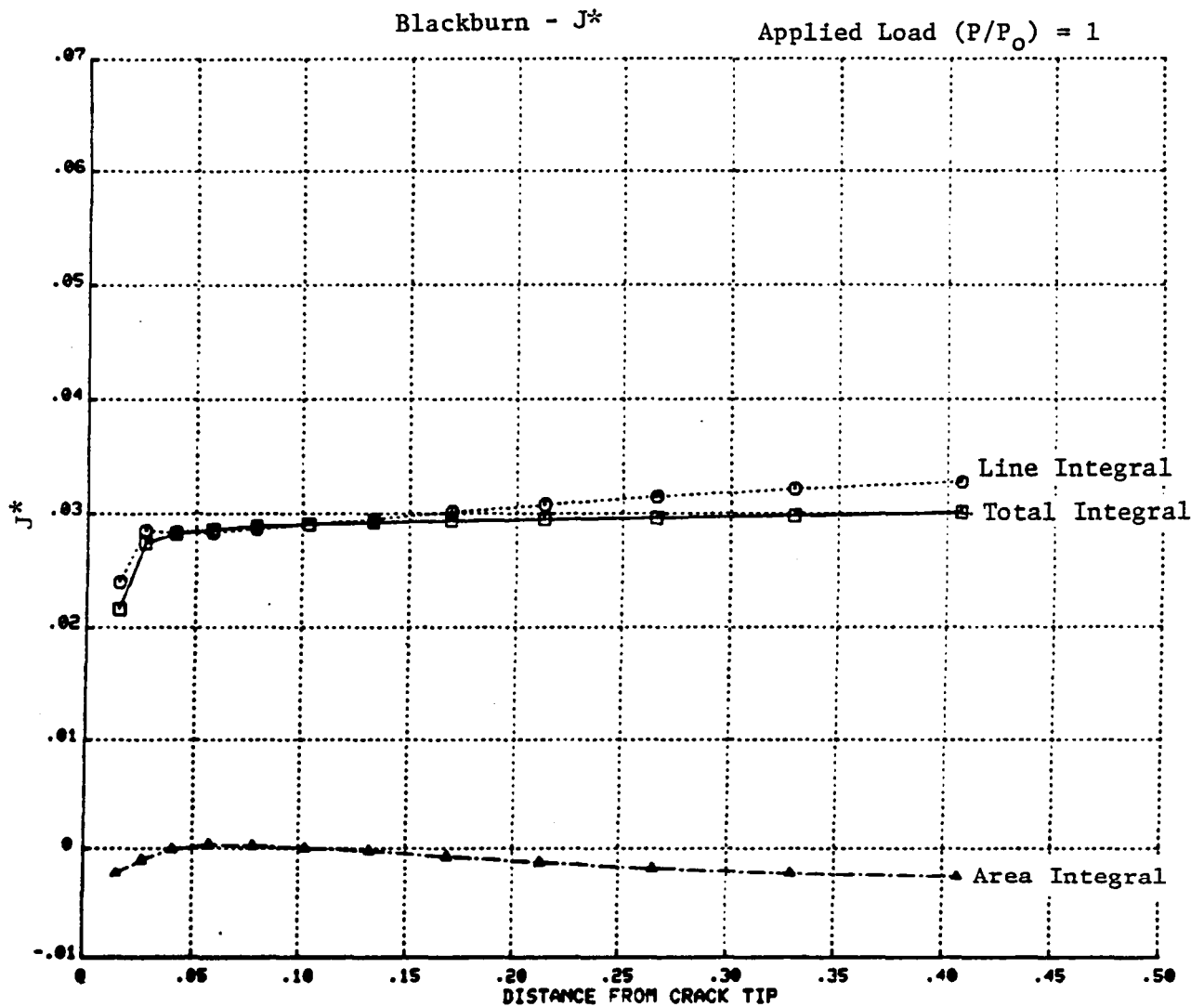


Figure 8. Blackburn J^* -Integral and Its Line and Area Integral Contributions Along Various Integration Paths for an Applied Load (P/P_0) of 1 in Compact Tension Specimen.

Blackburn - J^*

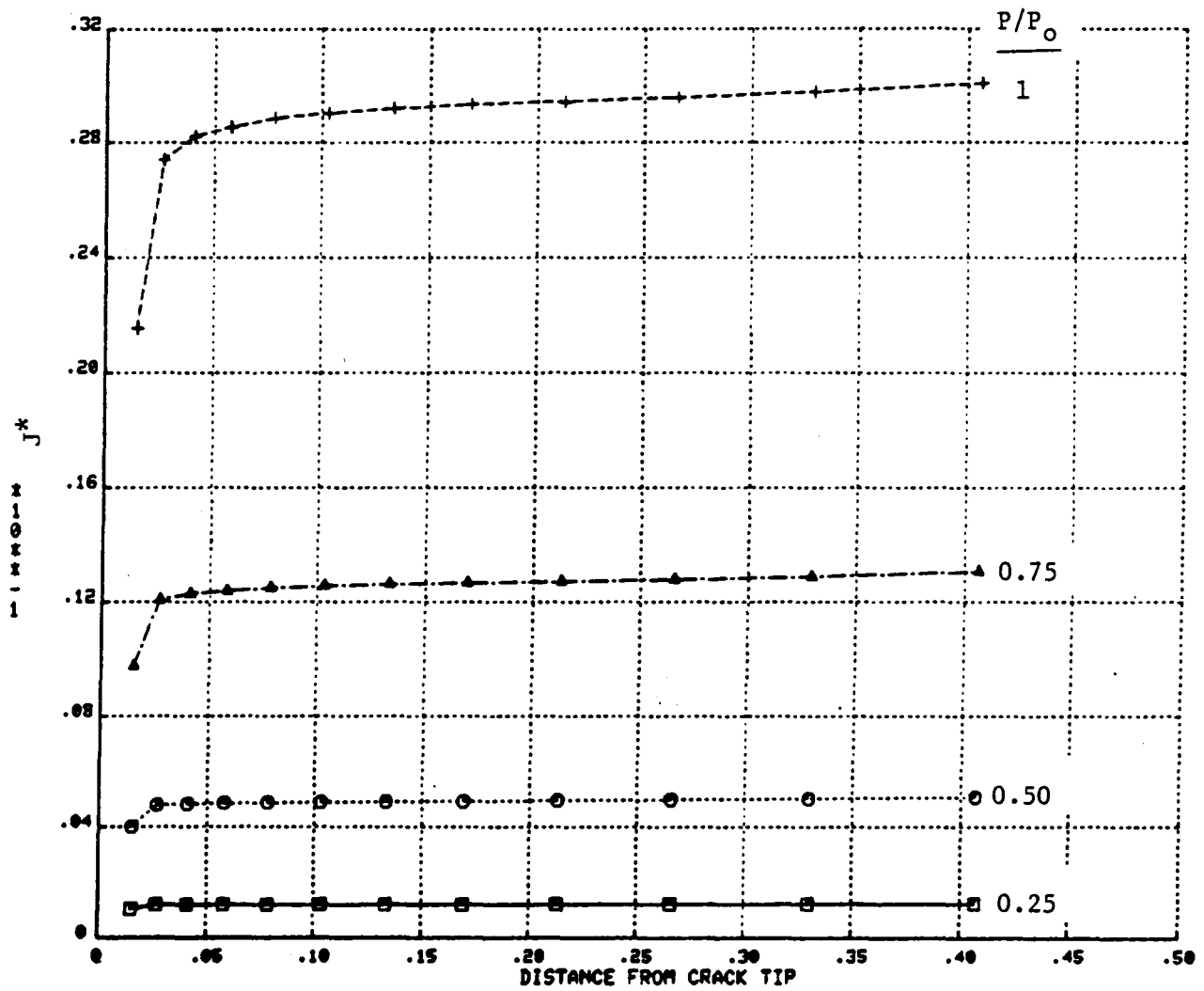


Figure 9. Blackburn J^* -Integral for the Four Load Steps for the Compact Tension Specimen.

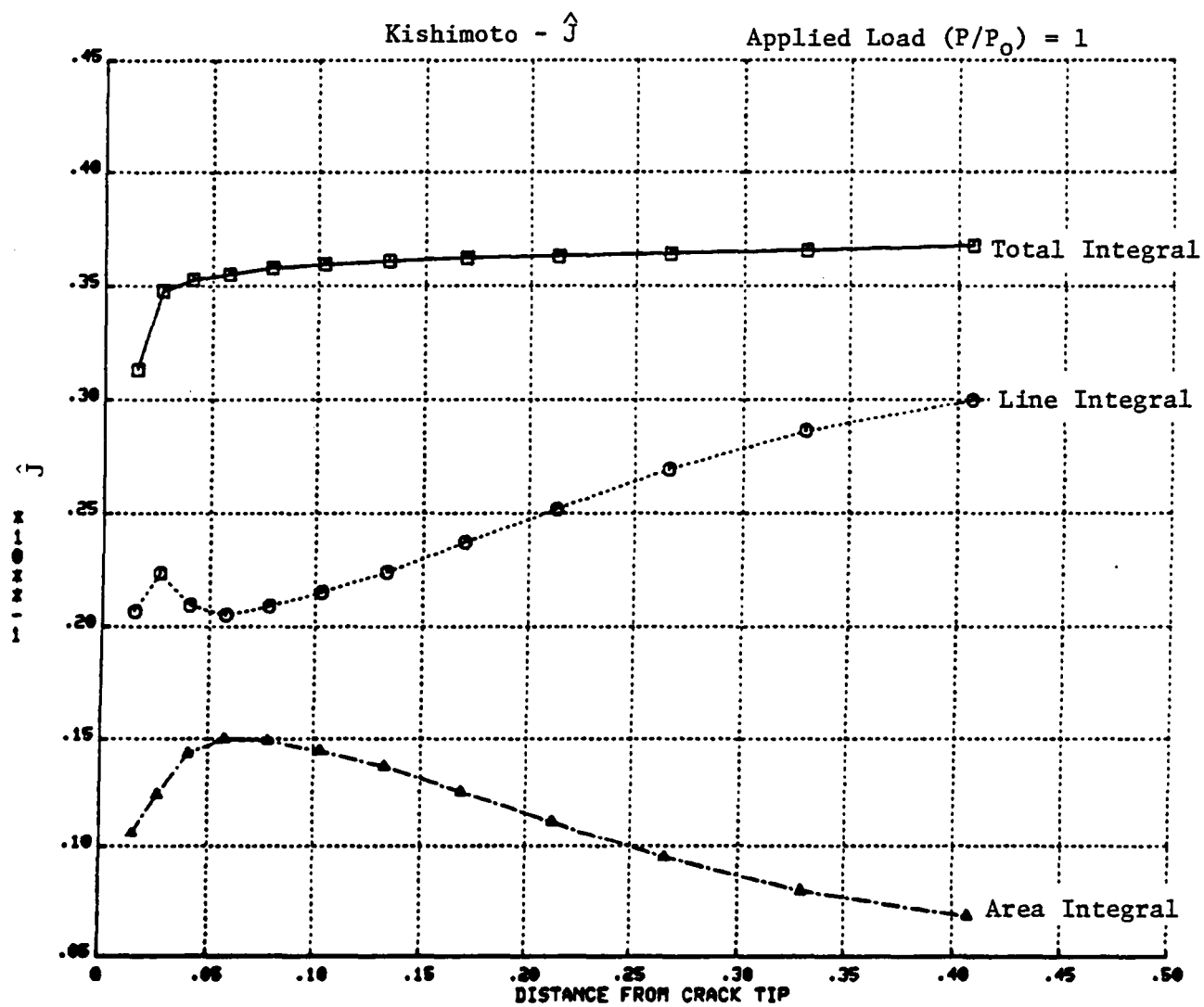
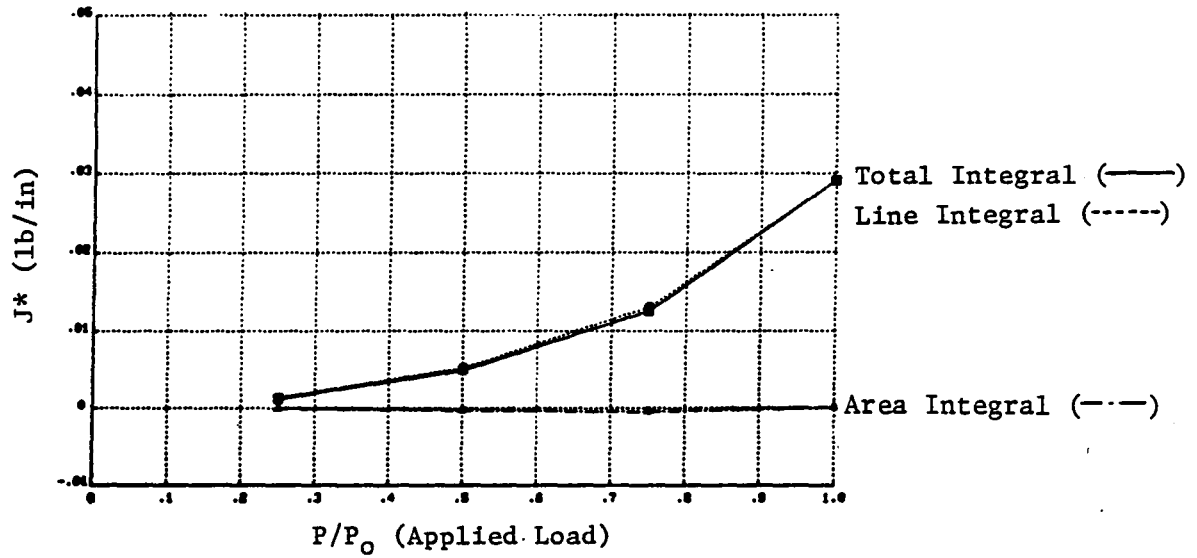


Figure 10. Kishimoto \hat{J} -Integral and Its Line and Area Integral Contributions Along Various Integration Paths for an Applied Load (P/P_0) of 1 on Compact Tension Specimen.

Blackburn - J^*



Kishimoto - \hat{J}

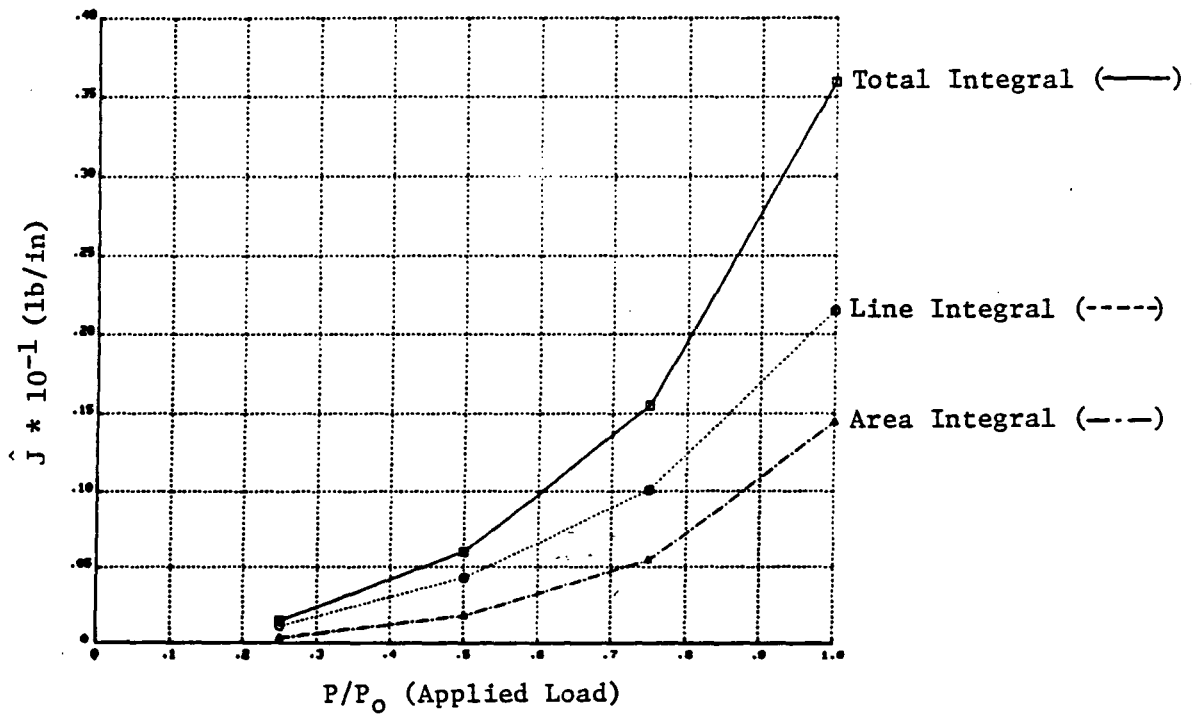


Figure 11. Comparison of Area and Line Integral Terms Contributions to Blackburn (J^*) and Kishimoto (\hat{J}) Integrals.

line and area integral contributions) are plotted as a function of the applied load. It is important to note that experimental measurements of a P-I integral are possible if the integral can be expressed as the rate of a potential or if it has only line integral contributions. On this basis it can be said that for the given Ramberg-Osgood material behavior in the given compact tension specimen geometry, it is much easier to perform experimental measurements for the J^* -integral as compared to \hat{J} -integral. Figure 12 shows the degree of path-independence for all the four load steps for Kishimoto \hat{J} -integral computations. Again, except for the integration paths nearest to the crack-tip, path-independence is obtained at all load levels.

The Atluri incremental P-I integrals, ΔT_p^* , were computed for loading up to the limit load and unloading to zero load. The eight loading and unloading steps are shown in Figure 13, in terms of an applied load versus load-line displacement plot. For each of the eight incremental load steps, the integrals ΔT_p^* and ΔT_p were computed and then summed to find the total integrals $T_p^*(= \sum \Delta T_p^*)$ and $T_p(= \sum \Delta T_p)$ at each value of applied load. Figure 14 shows the incremental ΔT_p^* -integral along various integration paths for all the eight loading and unloading steps in the compact tension specimen. It is evident that a uniform degree of path-independence is maintained for the four loading steps (1 to 4) up to the specimen limit load. However, for the four unloading steps (5 to 8), the degree of path-independence is not as good as during the loading steps. This observation is also noted in the total integral $T_p^*(= \sum \Delta T_p^*)$ values shown in Figure 15. Especially for the last two unloading steps (7 and 8), the degree of path-independence has somewhat deteriorated. Still, the T_p^* -integral values are within 15% of each other along various paths except for the paths very close to the crack tip. Similar observations are found in Figures 16 and 17 for the integrals ΔT_p and $T_p(= \sum \Delta T_p)$, respectively, during the loading and unloading steps.

In Figure 18, the Atluri integrals T_p and T_p^* are plotted as a function of the applied load. As expected for proportional loading, these two integrals have fairly identical values during the loading-up stage. However, for the inelastic unloading steps (5 to 8) the two integrals have considerably different values. The T_p -integral decreases for the unloading steps but its values always remain positive. Contrary to this, the T_p^* -integral has negative values for some of the unloading steps. This fact has also been observed by Atluri et al. (References 14,15) in recent investigations. Figure 19 shows the T_p and T_p^* integrals for displacement-controlled global loading and unloading steps in a compact tension specimen as reported in Reference 14 for plane-strain conditions. It can be seen in Figure 19 that T_p^* -integral for some of the unloading steps has negative values even though the global load acting on the specimen is tensile in nature with crack surfaces opened-up and having positive load-line displacements. Thus, a physical interpretation of T_p^* -integral in terms of an energy-like quantity is not possible for global unloading steps for the stationary cracks studied here.

A comparison of all P-I integrals under study in the present work is shown in Figure 20 for the first four monotonic loading steps shown in Figure 13. It can be seen that for the compact tension specimen studied, the Rice J -integral values are coincident with T_p -integral by Atluri, and the Blackburn

Kishimoto - \hat{J}

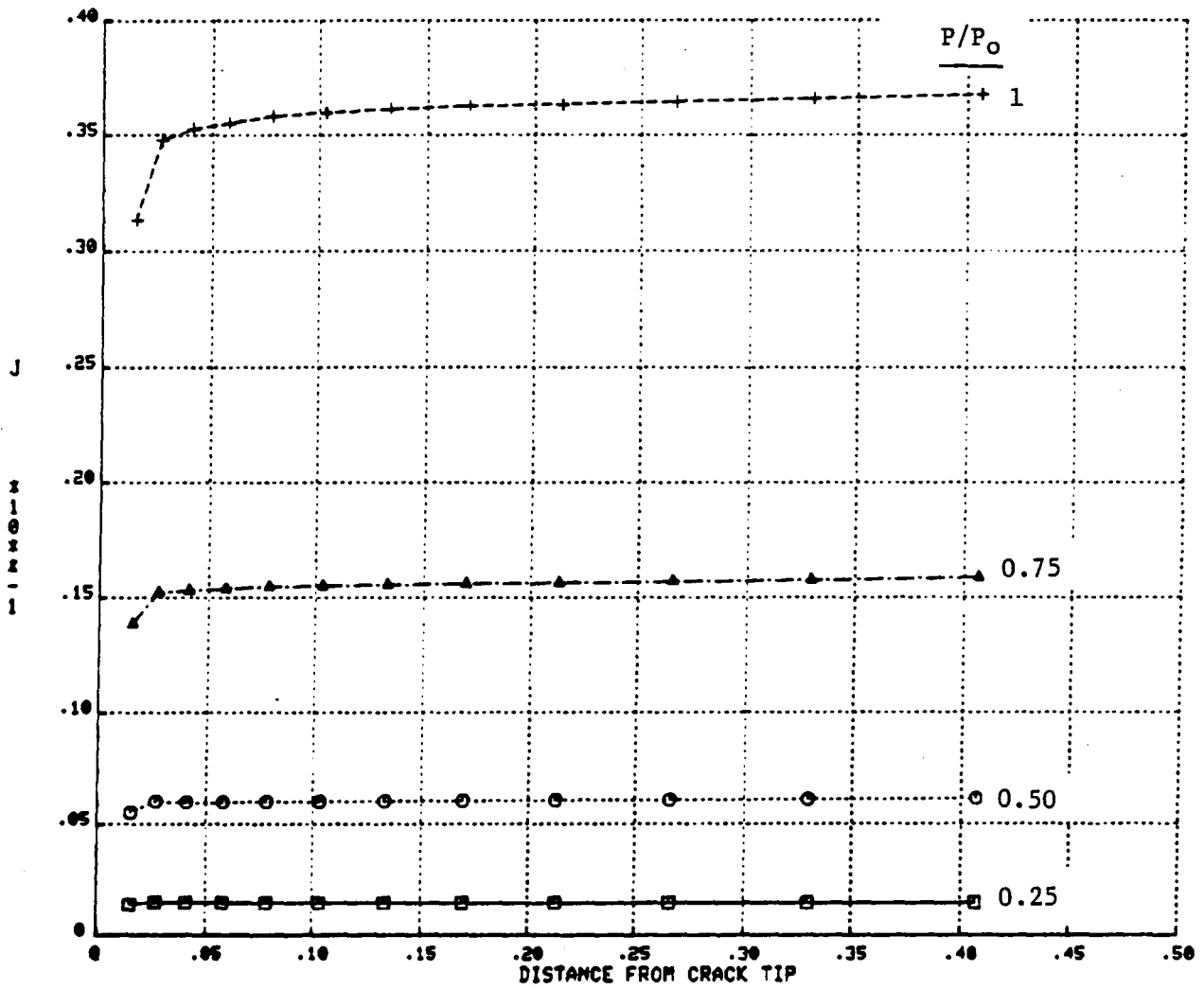


Figure 12. Kishimoto \hat{J} -Integral for the Four Load Steps for the Compact Tension Specimen.

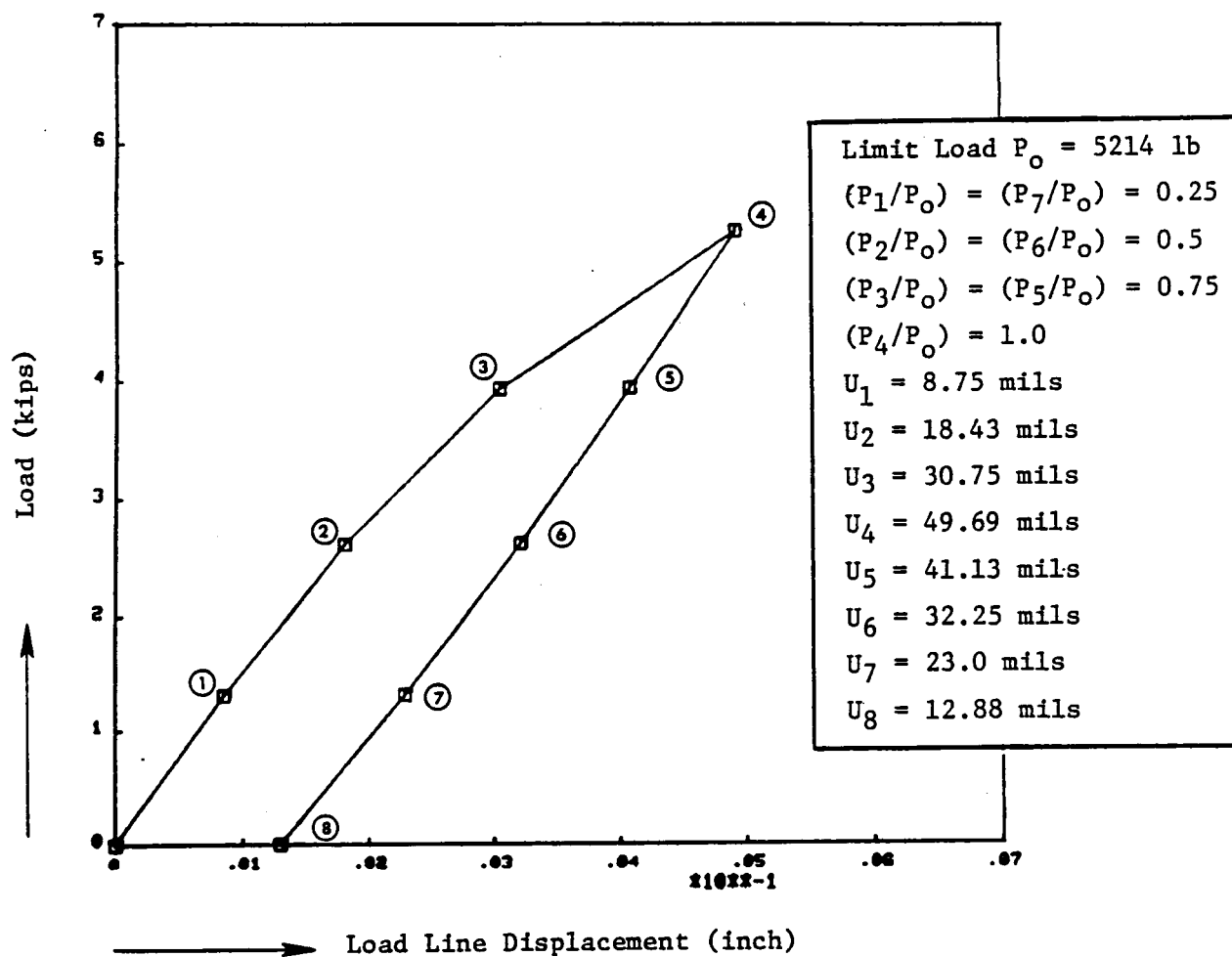


Figure 13. Load Versus Load Point Displacement for the Compact Tension Specimen at Various Load Steps.

ATLURI (ΔT_P^*)

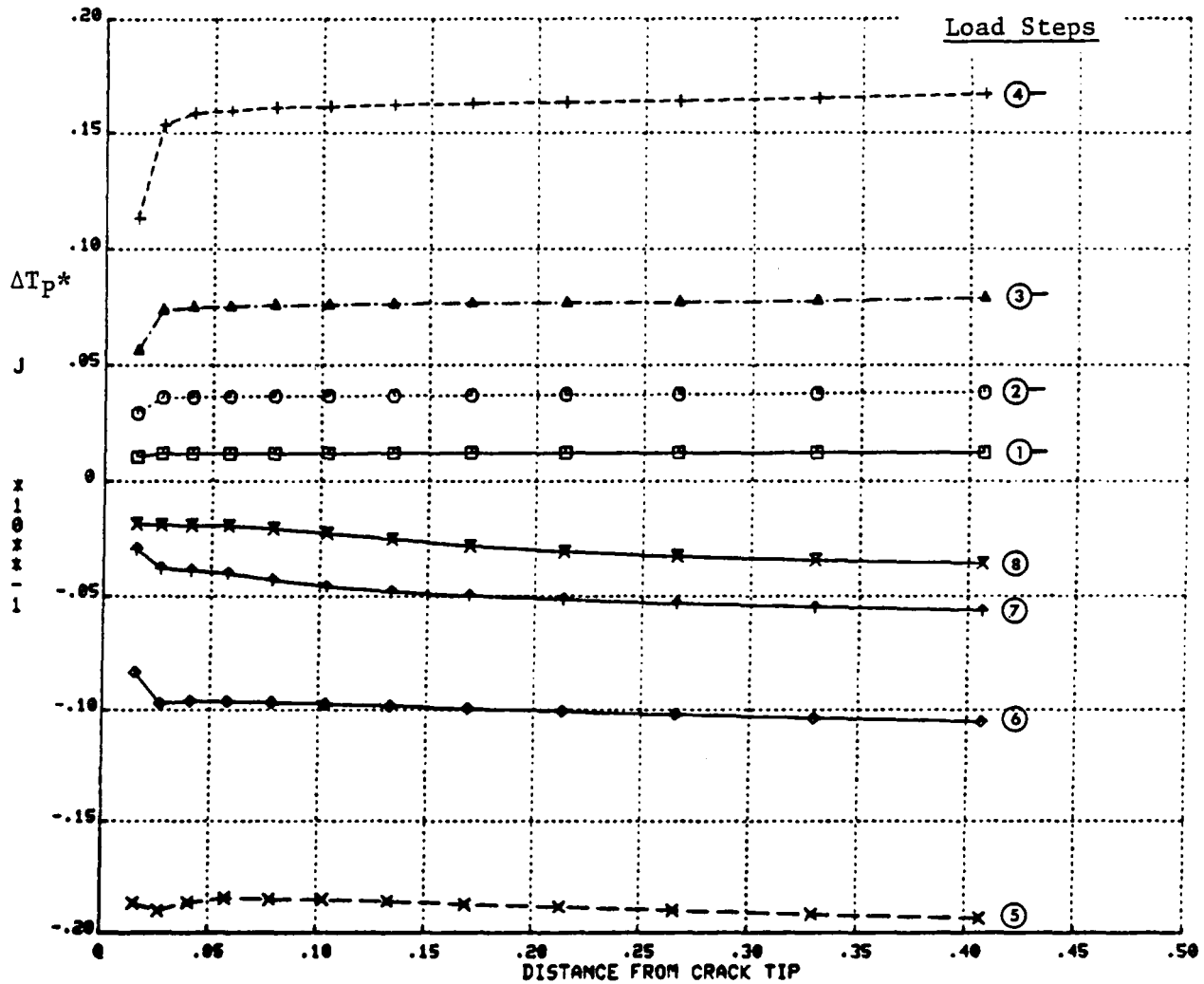


Figure 14. Atluri ΔT_P^* Incremental Integral Along Various Integration Paths for Loading and Unloading Steps on Compact Tension Specimen.

ATLURI (TP*)

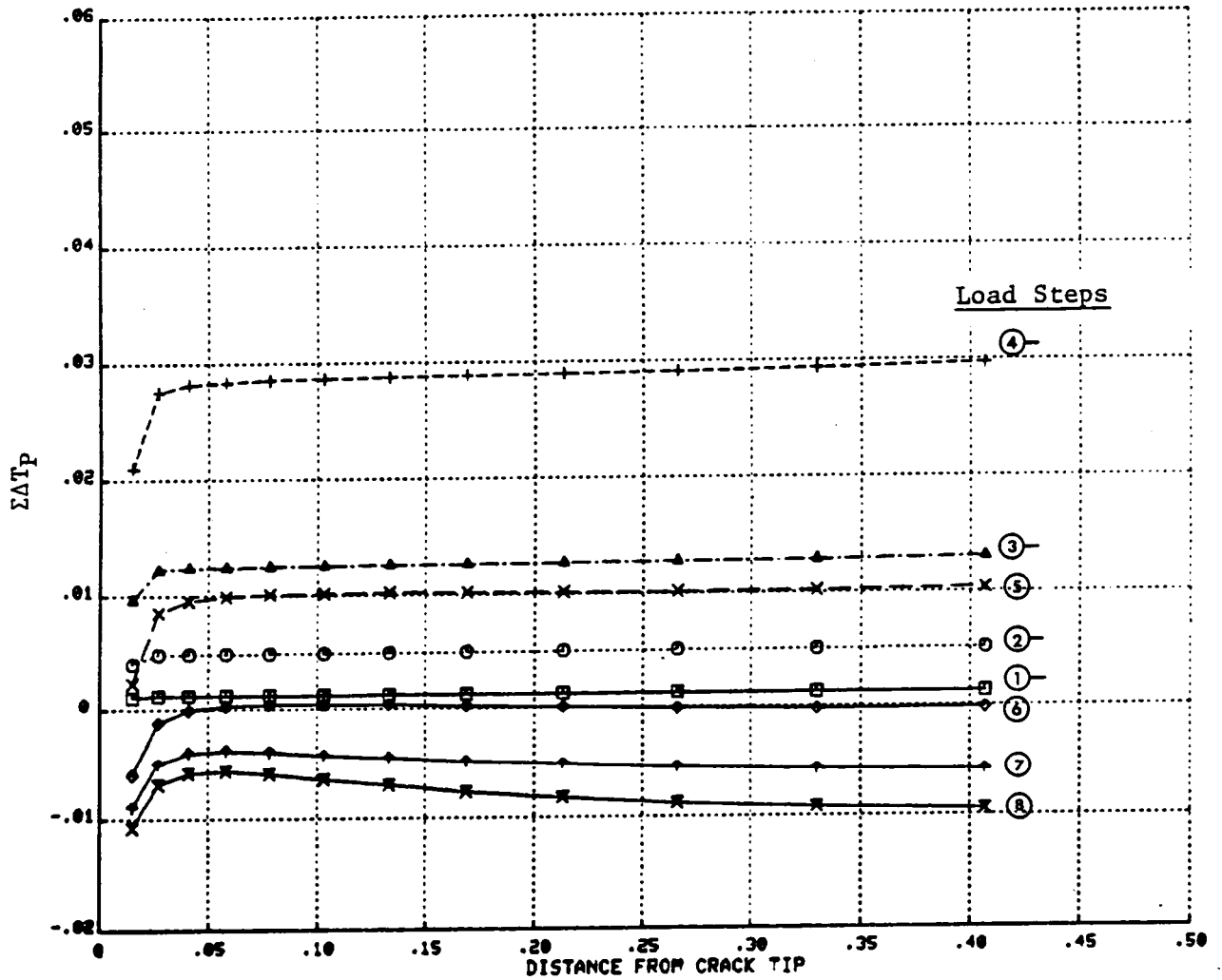


Figure 15. Atluri T_p^* -Integral ($=\Sigma \Delta T_p^*$) Along Various Integration Paths for Loading and Unloading Steps.

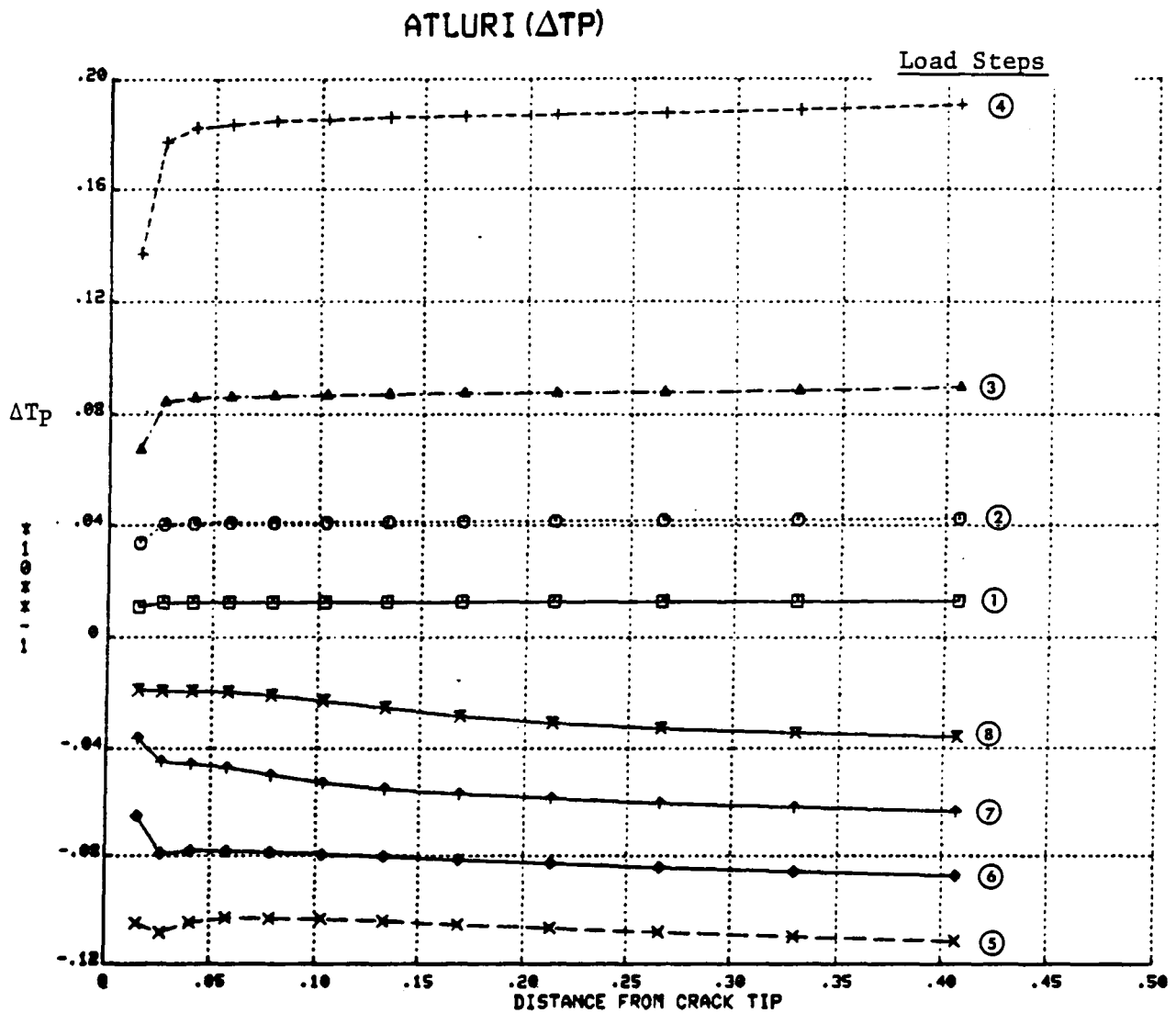


Figure 16. Atluri ΔT_P Incremental Integral Along Various Integration Paths for Loading and Unloading Steps on Compact Tension Specimen.

ATLURI (TP)

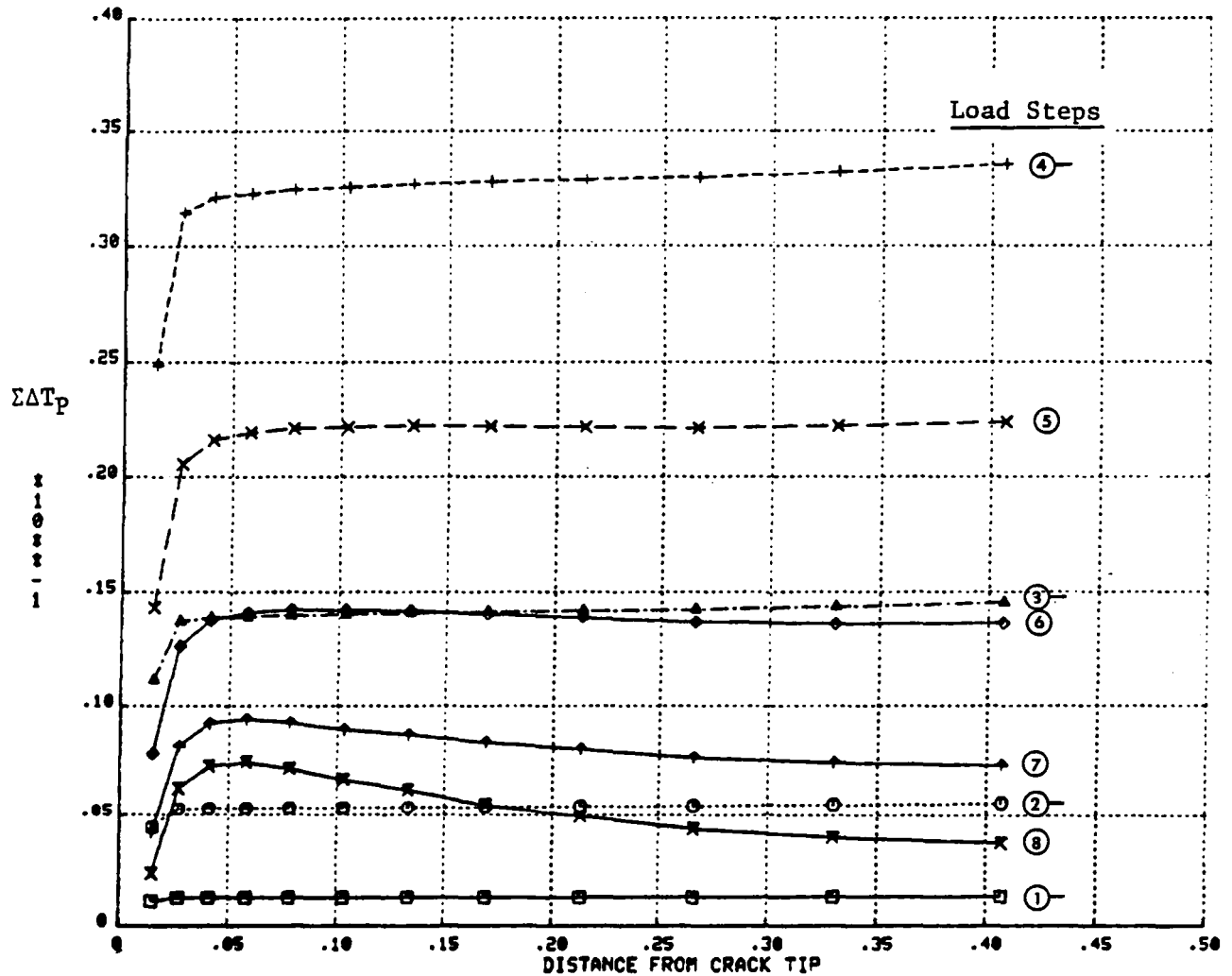


Figure 17. Atluri Tp-Integral ($=\Sigma\Delta T_p$) Along Various Integration Paths for Loading and Unloading Steps.

COMPARISON OF INTEGRALS T_P and T_P^*

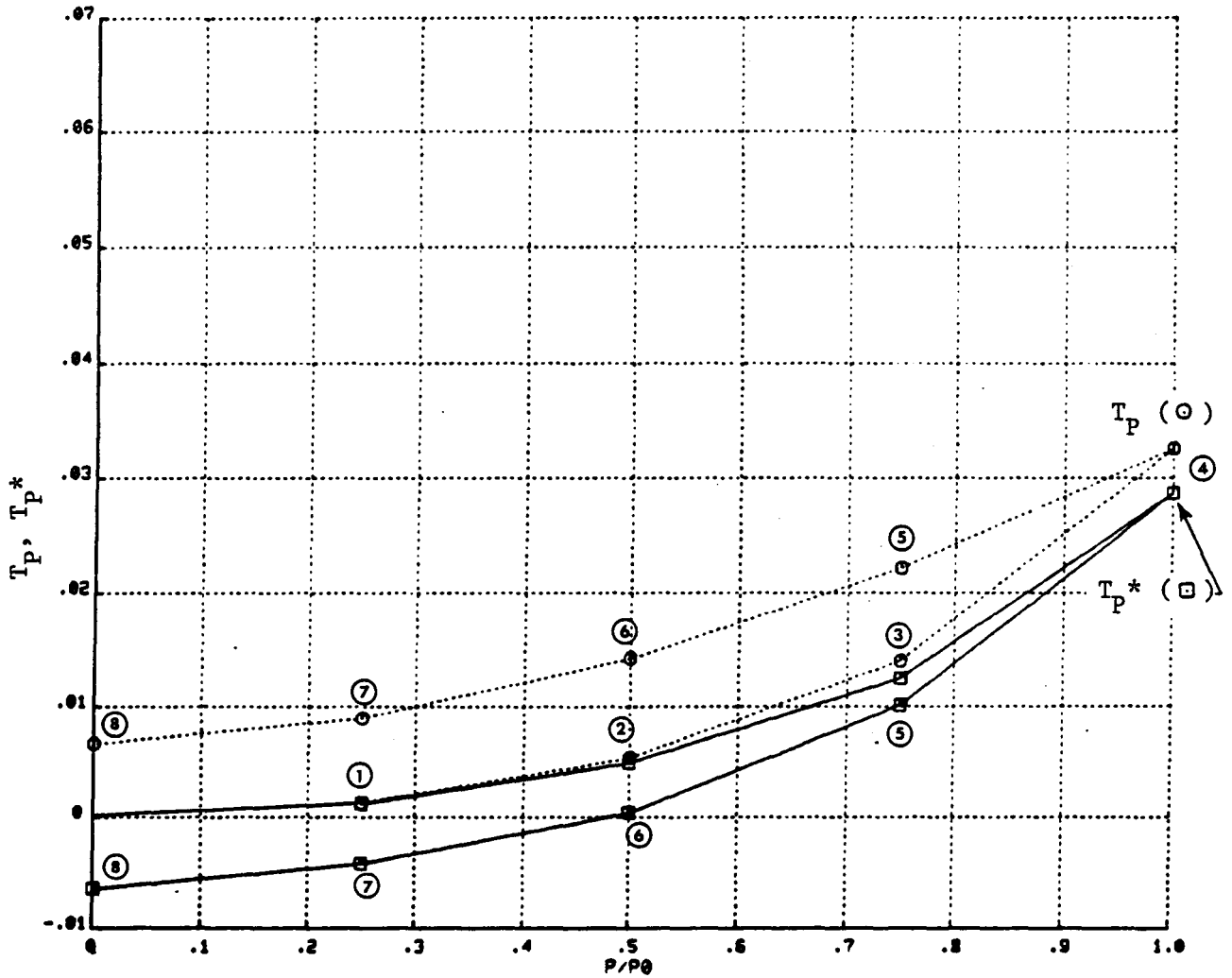


Figure 18. Comparison of Present Results for Atluri T_P and T_P^* Integrals as a Function of Applied Loading and Unloading Steps in Compact Tension Specimen.

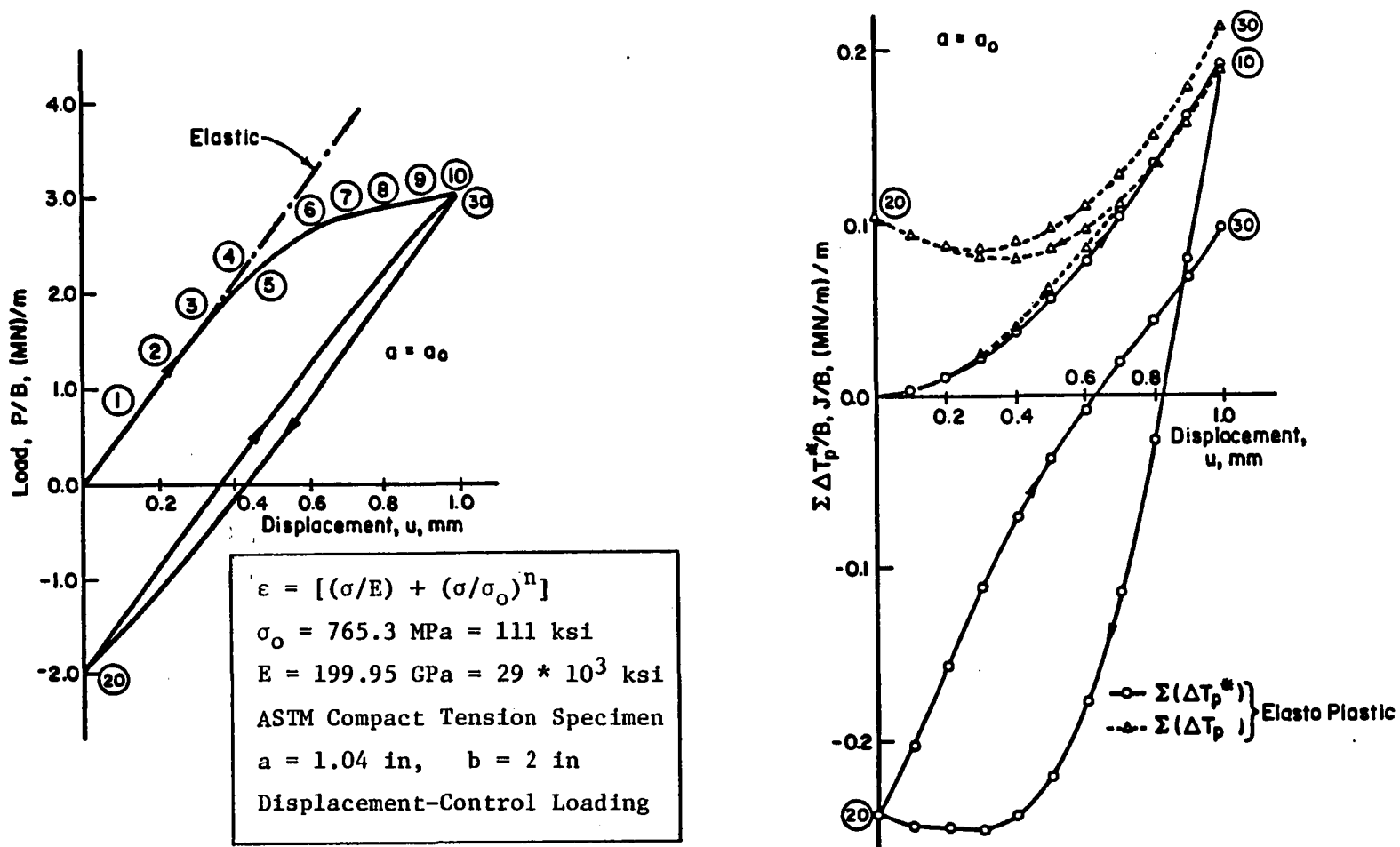


Figure 19. Atluri Integrals T_p and T_p^* for Loading and Unloading Steps in a Compact Tension Specimen Reported in Reference 14.

COMPARISON OF INTEGRALS

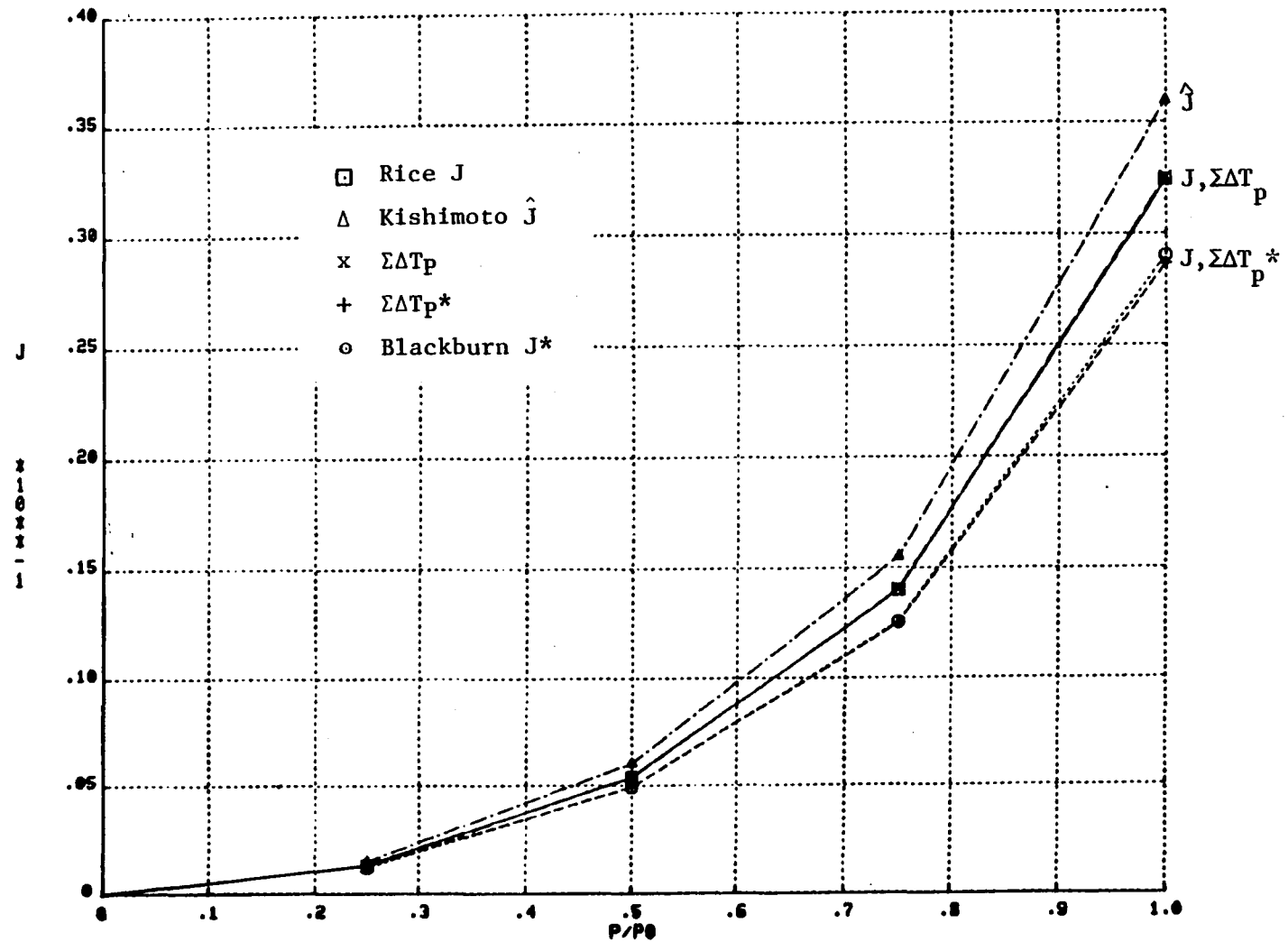


Figure 20. Comparison of Various P-I Integrals Obtained From Present Study for Loading Steps on Compact Tension Specimen.

J^* -integral values are very close to Atluri's Tp^* -integral. This may be due to the fact that the area integral terms in J^* , Tp , and Tp^* integrals have smaller contribution relative to the line integral terms for the example problem studied in this program. The Kishimoto \hat{J} integral represented an upper bound for all the P-I integrals studied.

3.3 MESH GENERATOR PROGRAM DEVELOPMENT

Initial development of a mesh generator computer program was completed for automatic generation of finite-element mesh-for-crack problems. This computer program allows a gradual transitioning of the mesh arrangement from a relatively coarse mesh in the remote stress field to very refined mesh near the crack area. Two basic types of mesh arrangement, the fan-type and square-type, are the developed options. The square-type mesh is generally considered to be more convenient for simulating crack growth behavior and crack closure phenomena. But the fan-type mesh provides better solution accuracy for near-crack-tip stress/strain field and its angular variation around the crack-tip for stationary cracks. However, it would be cumbersome to use the fan-type mesh for growing cracks since this mesh has angular rays focused at the crack tip.

Figure 21 shows the concept and an example of the square mesh generated for a single-edge crack specimen. It has major, minor, and transition layers of elements. Each major layer has square-type regions which are divided into triangular elements obtained by connecting one of the diagonals of each square. Minor layers represent the mesh refinement for the crack tip, and they are obtained by connecting both of the diagonals of pertinent square regions. The parameters l_1 and l_2 , measured from the crack tip, are used to get the number of minor layer elements within each major layer. Currently, the transition layers are set to reduce the element size by one-half in vertical direction only. This gives a uniform mesh refinement to the entire crack plane. To reduce the total number of elements, it is felt that the refined elements should be restricted into the crack region rather than the whole width of the specimen. To accomplish this, transition elements will also be needed in horizontal direction. This improvement in the mesh generator program is now under development.

Figure 22 shows the user-defined parameters needed for fan-type mesh generation. An example of the mesh generated is also shown in Figure 22. The parameters N_1 , N_3 , and N_5 define the total number of radial lines focused at the crack tip. Parameter N_4 defines how many segments these radial lines are to be subdivided into. This subdivision of the radial lines can be either linear (equal interval) or nonlinear. The example in Figure 22 shows a nonlinear subdivision with smaller segments near the crack tip.

A fan mesh was used to model the compact tension specimen for evaluating the P-I integral in the present work. However, it is planned to use extensively a square mesh to simulate crack growth behavior and crack closure phenomenon requiring crack tip node release and changes in crack surface boundary conditions. This would enhance numerical accuracy due to a fairly uniform distribution of element stiffnesses along the crack-growth path.

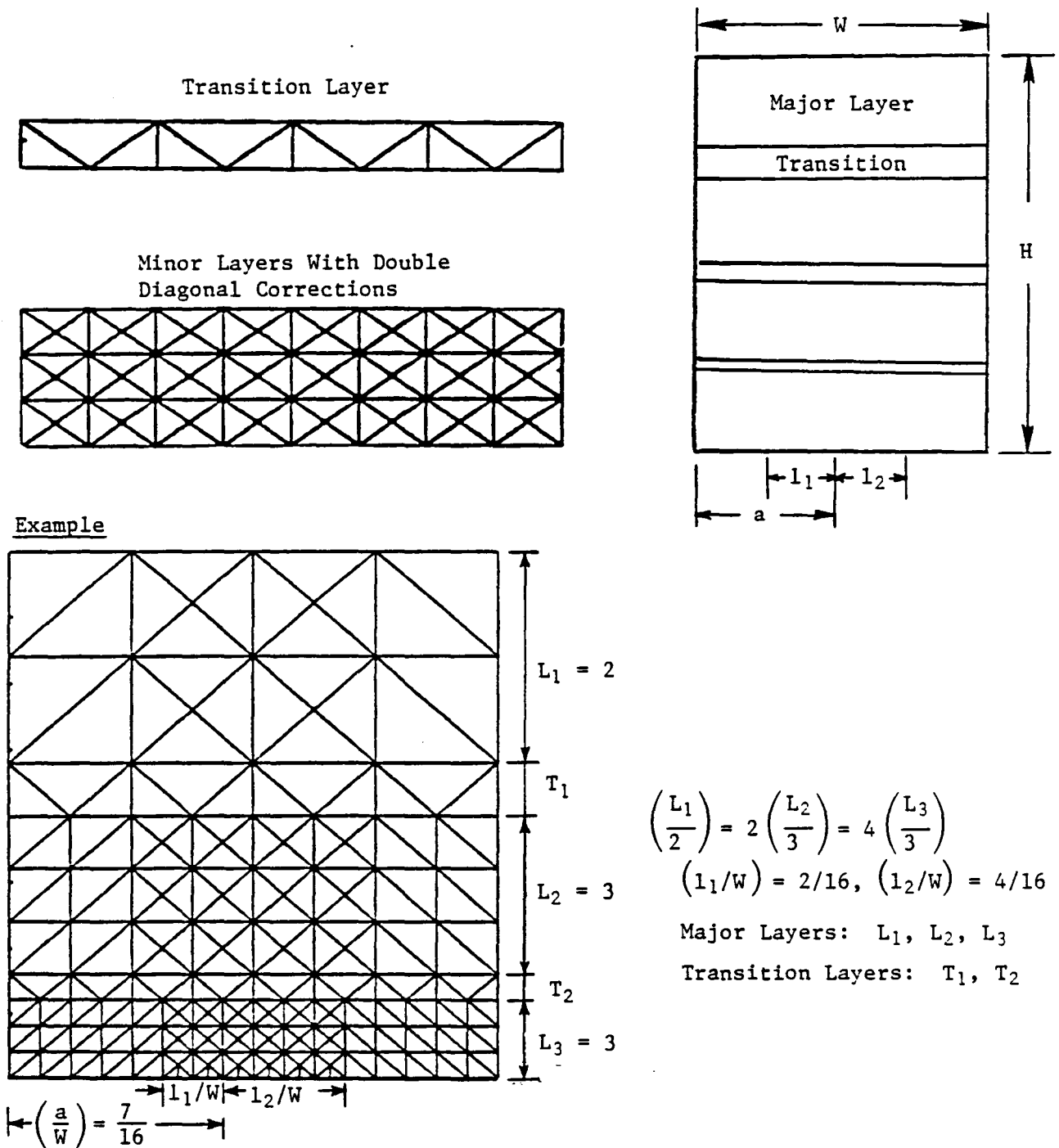
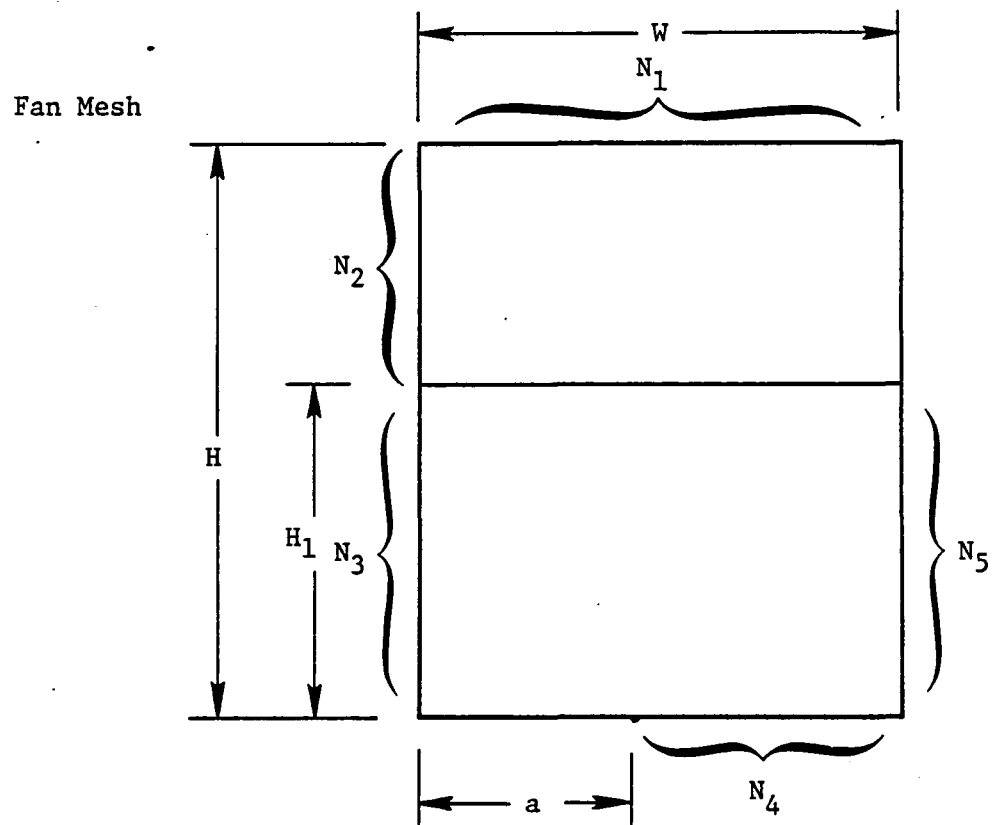


Figure 21. An Example of Square Mesh Generated for a Single Edge Crack Specimen.



Example:

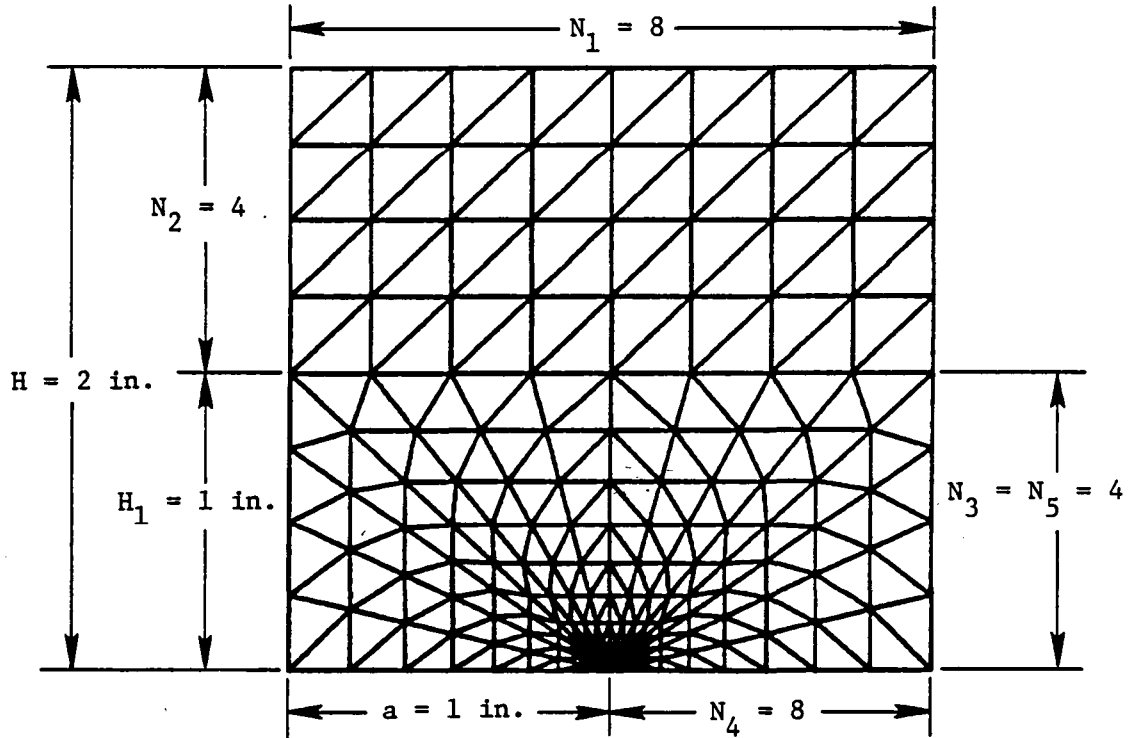


Figure 22. An Example of Fan Mesh Generated for a Single Edge Crack Specimen.

4.0 EXPERIMENTAL WORK

4.1 ANALOG MATERIAL

The purpose of the experimental portion of this investigation is to perform experiments that will determine the validity of the selected path-independent (P-I) integrals. The "analog" material was selected so that it could be tested at relatively low temperatures while retaining many of the important characteristics of a combustor liner material. Since significant thermomechanical testing will be performed, the selected alloy has to display a range of properties over a significant temperature range. The specific characteristics evaluated include:

- Significant variation in elastic modulus throughout the test temperature range
- Large changes in short-time creep rates throughout the test temperature range
- No metallurgical- or stress-induced phase transformations in the test temperature range
- Thermal conductivity conducive to perform thermal gradient and thermomechanical fatigue (TMF) tests.

Nickel-Base Alloy 718 was selected for this program, strengthened by γ' . It is metallurgically stable up to temperatures approaching 700° C (1292° F), and has physical properties (thermal expansion and conductivity) similar to nickel-base combustor alloys. In this study it is planned to perform crack growth evaluations over the temperature range from 427° C (800° F) to 649° C (1200° F). Table III shows the range of elastic modulus and creep properties throughout this temperature range. The modulus varies by approximately 10%, and the creep rates, estimated by the time to creep as 0.2%, vary by at least four orders of magnitude. Thus, Alloy 718 meets the requirements for an analog material. This selection was approved by the NASA Program Manager.

Alloy 718 plate was procured for use in this program. The plate has a nominal thickness of 22.2 mm (0.875 inch) and was procured in 13 pieces, each measuring 381 mm (15 inches) by 406 mm (16 inches). This plate was produced by Cabot Corporation from heat 2180-1-9836. The ladle composition and specification for Alloy 718 are compared in Table IV. This composition falls within the specified limits.

This material was supplied in a mill-annealed condition. The plates were subsequently solution-treated and aged at the General Electric Engineering Material Technology Laboratory (EMTL) in a vacuum furnace under computer control. The plates were solution-treated at 968° C (1775° F) for one hour at temperature, and then cooled to room temperature. They were then aged at 718° C (1325° F), for eight hours at temperature, cooled at 56° C/hr (100° F/hr) to 621° C (1150° F), where they were held for eight hours. Two

plates were heat treated simultaneously. Each heat treatment run was monitored with multiple thermocouples. In the first run (containing only one plate) the aging time exceeded the requested time. For this reason, the plate received a second solution treatment and age cycle. This was not an unusual occurrence. However, to eliminate any potential effects, this plate was used only for specimen development. The remaining plates were heat treated successfully.

Table III. Variation of Alloy 718 Elastic Modulus and Creep Properties with Temperature.

	427° C (800° F)	538° C (1000° F)	649° C (1200° F)
Young's Modulus (MPa)	182	175	166
Time to Creep 0.2% At 700 MPa (Hours)	---	30,000	2

4.2 TEST MATRIX

The purpose of the testing program is to provide data to support analytical activities. These tests are intended to develop this methodology rather than develop basic material properties. The testing will be performed as part of three tasks:

- Task III - Analog Material (constitutive properties)
- Task VII - Isothermal and Thermal Mechanical Fatigue (TMF) crack propagation analog material
- Task VIII - Crack propagation with thermal gradient analog material.

The test matrix for each task will be discussed separately.

4.3 TASK III - ANALOG MATERIAL (CONSTITUTIVE PROPERTIES)

The purpose of testing in this phase is to develop the mechanical property data for use in the finite-element calculations in subsequent phases. The tests include tensile, creep, and cyclic tests. The tensile/creep and cyclic fatigue specimens are axisymmetric geometries with a nominal diameter of 0.25 inch and a nominal gage length of 1 inch. The tensile/creep specimens (Figure 23) have threaded grips, while the cyclic specimens (Figure 24) have

Table IV. Composition of Alloy 718 Plate.

(Weight Percent)

<u>Element</u>	<u>Specification</u>	<u>Ladle Analysis</u>
C	0.02-0.08	0.06
Mn	0.35 Max	0.17
Si	0.35 Max	0.17
S	0.015 Max	< 0.002
P	0.015 Max	0.006
Cr	17.0-21.0	17.92
Fe	15.0-21.0	18.32
Co	1.0 Max	<0.10
Mo	2.80-3.30	3.03
Nb+Ta	4.75-5.50	5.11
Ti	0.75-1.15	1.12
Al	0.30-0.70	0.45
B	0.006 Max	0.002
Cu	0.30 Max	0.03
Ni	50.0-55.0	53.63

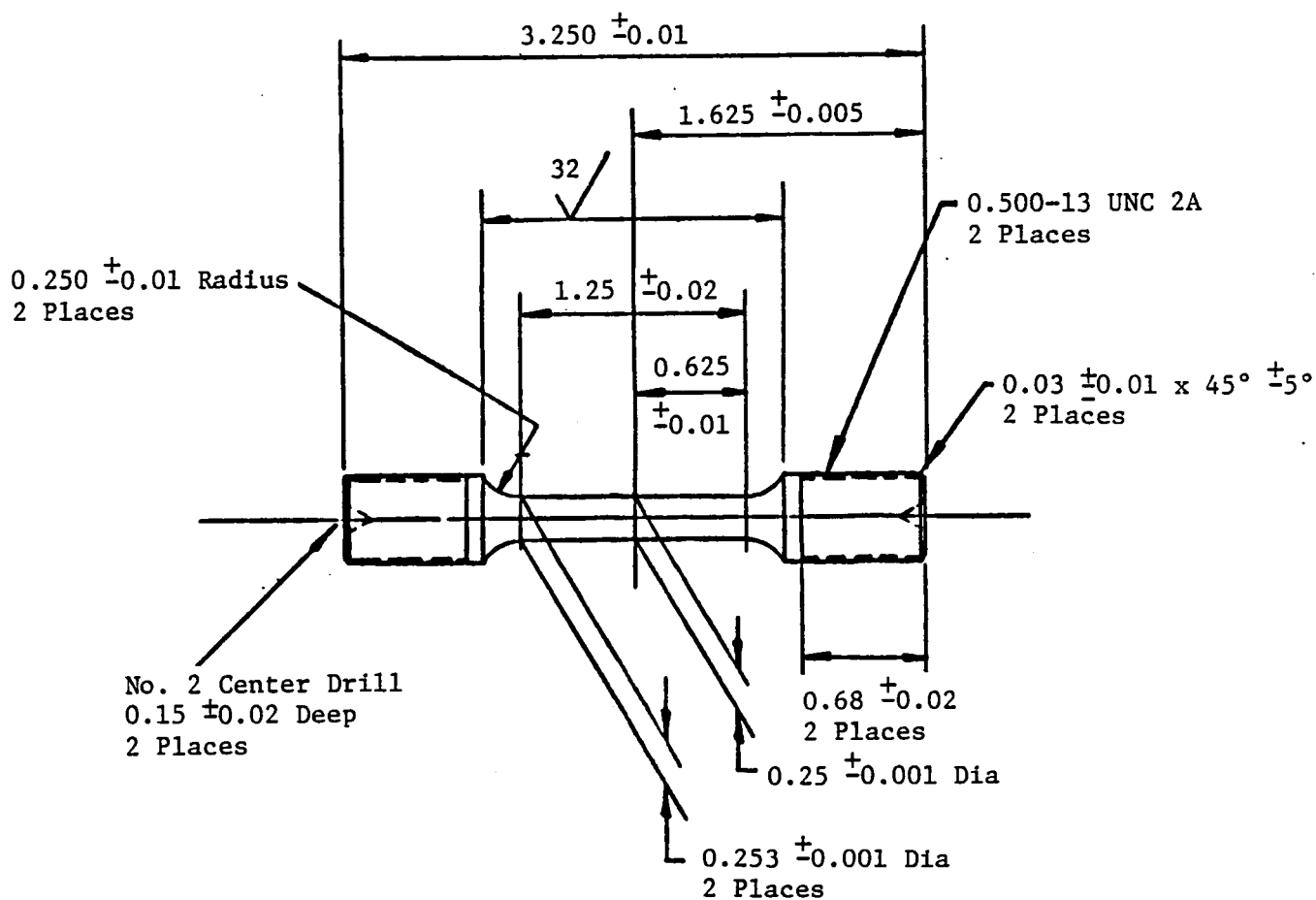


Figure 23. Specimen Bar Smooth Tensile, Rupture or Creep Rupture, 0.250 Gage Diameter.

buttonhead grips. The latter situation permits better load reversal and alignment, especially for compressive loads.

The tensile and cyclic tests will be run at several strain rates so that an appropriate constitutive model can be developed. Based on other work at General Electric, it is not anticipated that Alloy 718 will show extensive strain rate sensitivity for the conditions used in this program.

Table V lists the test matrix for these tests. The tensile tests will be conducted at three strain rates. The cyclic tests will be conducted at two strain rates. Duplicate creep tests will also be performed. The slowest strain rates correspond to the strain rates to be used in the Task VII and Task VIII crack propagation tests. All tests will be performed in closed loop equipment under strain control. The data from the cyclic tests will be acquired using an automated system that monitors both maximum stress and hysteresis information (Reference 16).

The strain ranges for the cyclic tests were determined based on a single 538° C (1000° F) test conducted using a constant strain amplitude block sequence. The test had an A_e ratio (alternating strain/mean strain) of infinity (zero mean strain), with a triangular wave shape and a strain rate of $2.0 \times 10^{-4} \text{ sec}^{-1}$. Each block contained 15 cycles. The strain range in the first block was 0.5%. The strain range in each subsequent block was increased by 0.5%. The test was continued until buckling occurred when the strain range was 4%. Figure 25 shows the variations in plastic strain range with total strain range for this test. Based on these data, the total strain ranges selected for the cyclic constitutive tests were 1.15%, 1.7%, and 3.5%. This corresponds to plastic strain ranges of approximately 0.2%, 0.7%, and 2.4%.

The highest strain range is intended to provide constitutive data for use in the finite-element calculations near the crack tip.

4.4 TASK VII - ISOTHERMAL AND TMF CRACK PROPAGATION, ANALOG MATERIAL

The purpose of the tests in this task is to provide input data and verification of the path-independent integral approach used in this investigation. These tests are designed to document the influence of temperature, strain range, mean strain, thermal cycling, and specimen geometry/loading on the crack propagation rates.

4.4.1 Specimen Design

One of the challenges of this program is to design crack-growth specimens that are capable of remote strain (displacement) cycling while experiencing bulk cyclic plasticity. The specimen should be two-dimensional to facilitate finite-element modeling. The primary specimen selected for this program was the single-edge-notch specimen shown in Figure 26. This specimen has a thickness of 2.54 mm (0.1 inch) to promote rapid heating and cooling during thermo-mechanical fatigue (TMF) cycling. Pin-loaded SEN specimens with this gage

Table V. Task III Test Matrix.

Test Type	Specimen Geometry	Temperature, ° F	Strain Rate, sec ⁻¹	Strain Range
Tensile	Axisymmetric	$\left(\begin{array}{c} 70 \\ 800 \\ 900 \\ 1000 \\ 1100 \\ 1200 \end{array} \right)$	$\left\{ \begin{array}{l} 2 \times 10^{-4} \\ 1 \times 10^{-3} \\ 5 \times 10^{-3} \end{array} \right\}$	---
	Tensile/Creep (Figure 23)			---
			---	---
			---	---
			---	---
Creep	Axisymmetric	$\left(\begin{array}{c} 1000 \\ 1100 \\ 1200 \end{array} \right)$	---	$\left\{ \begin{array}{l} \text{To} \\ \text{Be} \\ \text{Selected} \end{array} \right\}$
• Duplicate Tests	Tensile/Creep (Figure 23)		---	

Cyclic	Axisymmetric	$\left(\begin{array}{c} 800 \\ 1000 \\ 1100 \\ 1200 \end{array} \right)$	---	$\left(\begin{array}{c} 0.0115 \\ 0.017 \\ 0.035 \end{array} \right)$
• $A_\varepsilon = \infty$	Cyclic		$\left\{ \begin{array}{l} 2 \times 10^{-4} \\ 5 \times 10^{-3} \end{array} \right\}$	
• Triangle	(Figure 24)			
Wave				
Shape				

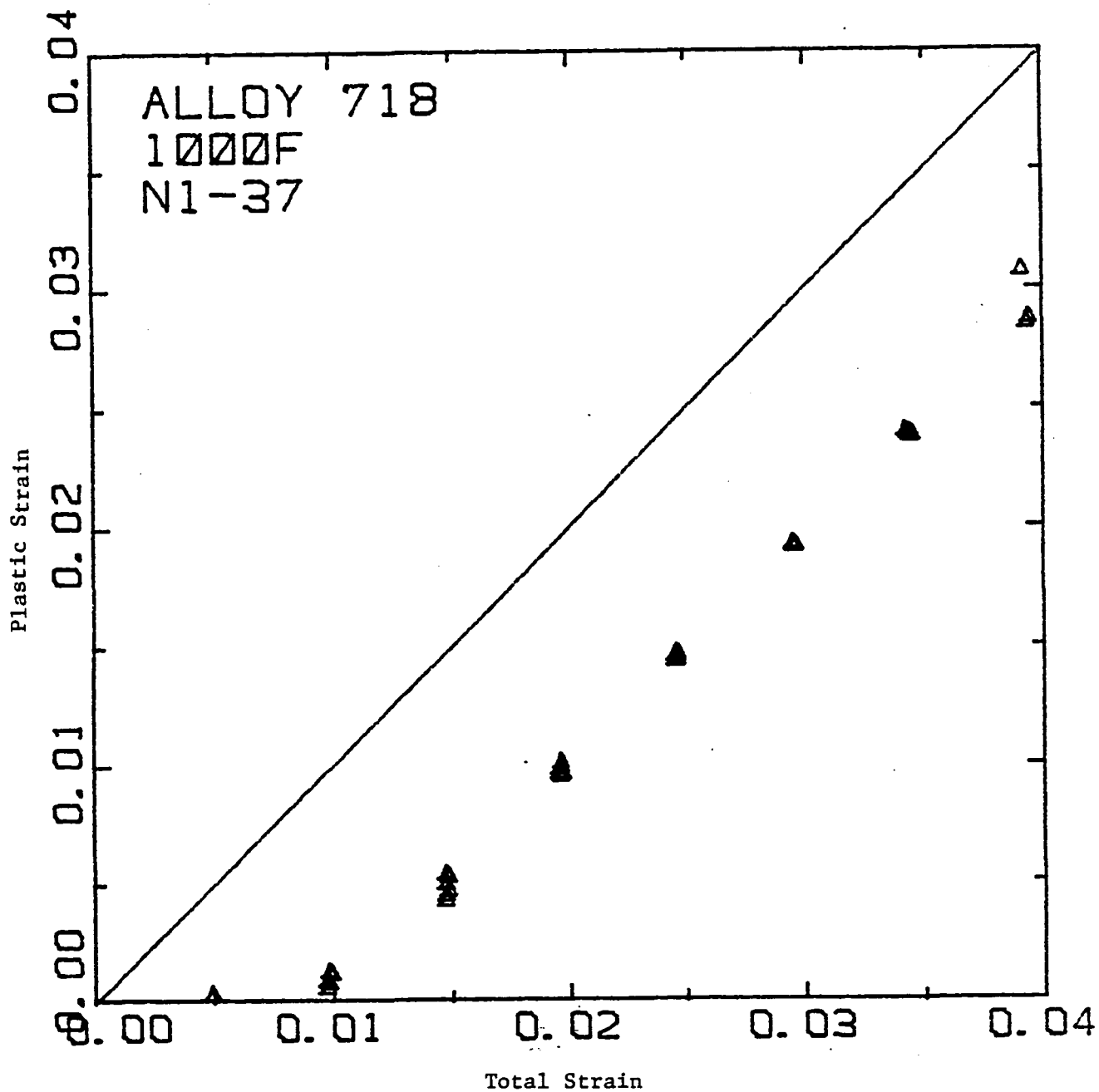


Figure 25. Variation of Plastic Strain Range With Total Strain Range for Alloy 718 at 1000° F With $\Delta_{\epsilon} = \infty$.

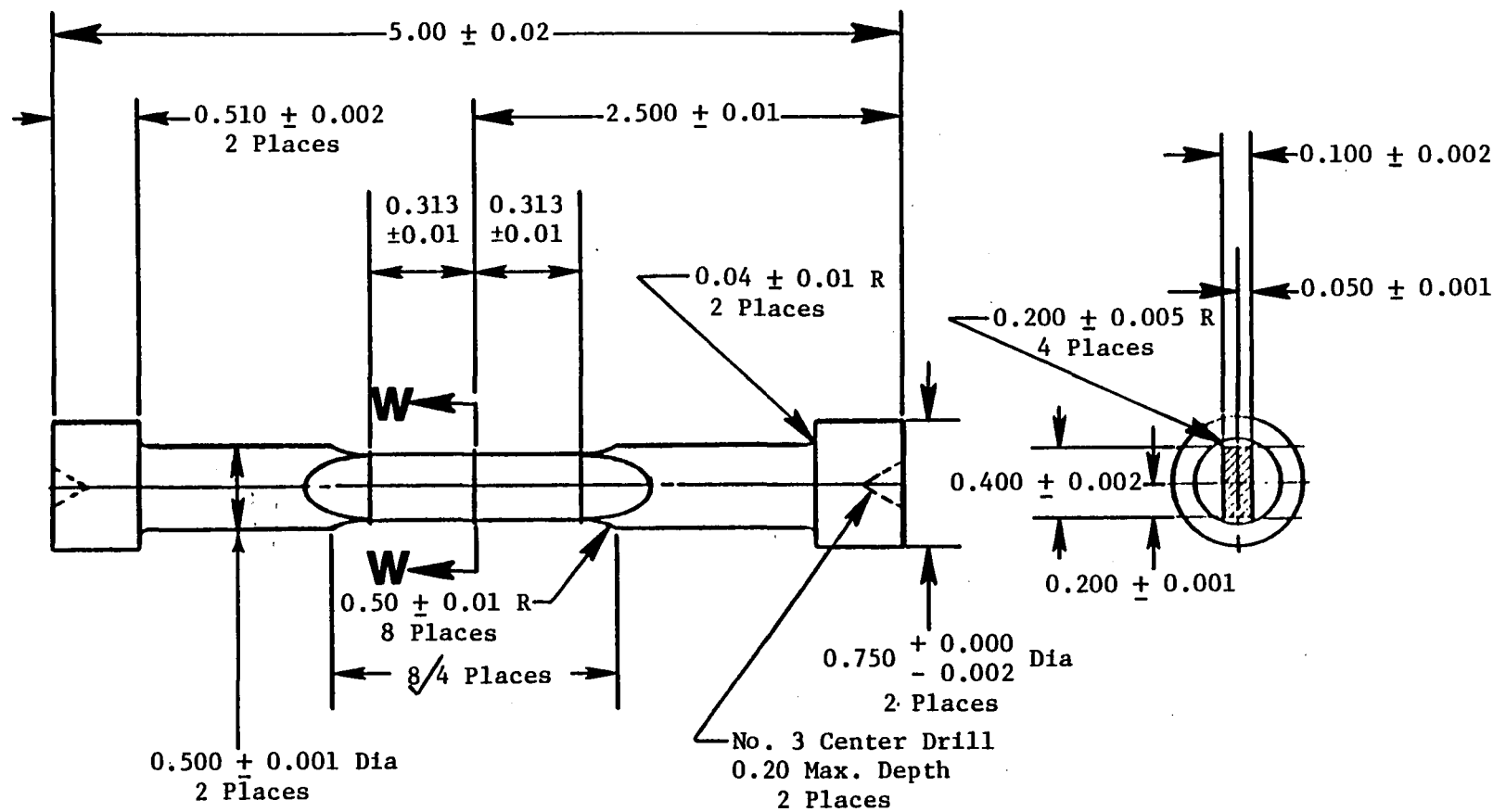


Figure 26. Buttonhead Single Edge Notch (SEN) Specimen.

section geometry have previously been used by General Electric to determine the linear elastic fracture mechanics crack growth properties of a wide variety of superalloys over a range from room temperature to 1800° F (References 17, 18). The modification of the specimen from pin to buttonhead loading was made to accommodate cyclic loading with compressive loads.

A series of SEN specimens were designed with gage lengths of 28.5, 22.2, and 15.9 mm (1.128, 0.875, and 0.625 inches) to evaluate resistance to buckling. The specimens were cyclically tested under either load or stroke control with the mean value of the control variable at zero ($A = \infty$). The range of stroke or load was gradually increased until buckling occurred. For the longest gage length geometry room temperature, buckling occurred at approximately 110 ksi. Based on elastic dimensionless analysis, the gage length was reduced to 22.2 mm. It was estimated that the buckling stress would be 175 ksi. At room temperature, the buckling stress was 177.8 ksi. At 1200° F, duplicate buckling tests were performed which yielded buckling stresses of 124.3 and 123.3 ksi. Based on previous data, this buckling stress is marginal for performing tests with cyclic plastic strain. From elastic dimensionless buckling analysis, it is estimated that gage length must be reduced to 15.9 mm to achieve 1200° F buckling stresses of 175 ksi. The results of a load control buckling test were very promising. Therefore, a crack propagation test was performed with the 15.9 mm gage length geometry at 1200° F with the largest strain range (1.7%) planned for use in this program. A 0.5-inch extensometer was placed in the center of the 10.2 mm wide face of a SEN specimen with a 0.1 mm deep EDM slot across one side of the 2.5 mm thickness. The specimen was cycled in strain control with A_ϵ of infinity at a strain rate of 2×10^{-4} /s.

A crack nucleated out of the EDM notch and propagated across the entire specimen. The hysteresis loop monitored during the test can be characterized into 3 groups. Very early in the test, perceptible softening was on each cycle as shown in Figure 27a. After some 20 cycles, the softening was not as rapid, and the loops had the classical appearance shown in Figure 27b. Cusps started to form as the crack propagated through the specimen, and the maximum stress diminished with each successive cycle. An example of this type of loop is shown in Figure 27c. Visual observation of the crack showed 45° shear bands emanating from the crack tip toward the unnotched free surface. These were observed over a wide range of crack lengths, but no remnants could be observed after completing the test. The fracture surface of this specimen was extremely flat and showed no evidence of shear lip or crack front tunneling.

An axisymmetric, smooth fatigue specimen was tested under identical test conditions. Examples of the initial hysteresis loop and the more stabilized loops are shown in Figures 28a and 28b, respectively. They have similar shape and magnitudes to the loops from the SEN specimen (Figures 27a and 27b). Figure 29 shows the variation in maximum and minimum stress with cycle number in the SEN and cyclic tests. Early in the test, when the crack length in the SEN specimen was short, both specimens showed similar constitutive responses. After approximately 30 cycles, the SEN specimen loops started to cusp. As shown in Figure 29, the minimum stress remained constant but the maximum stress started to decrease. At the end of the test (Cycle 68), the maximum

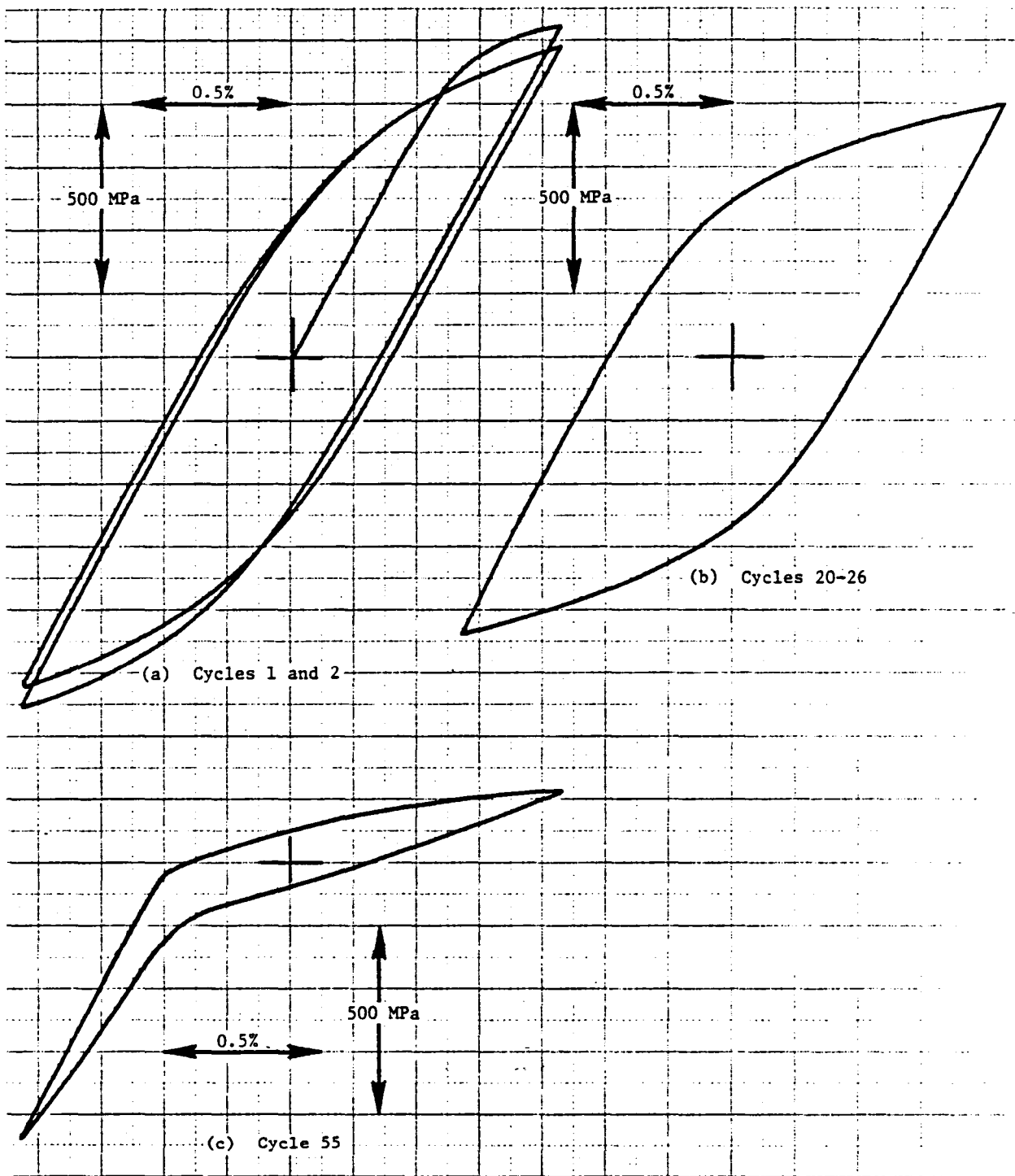


Figure 27. Examples of Hysteresis Loops in SEN Crack Propagation Tests.

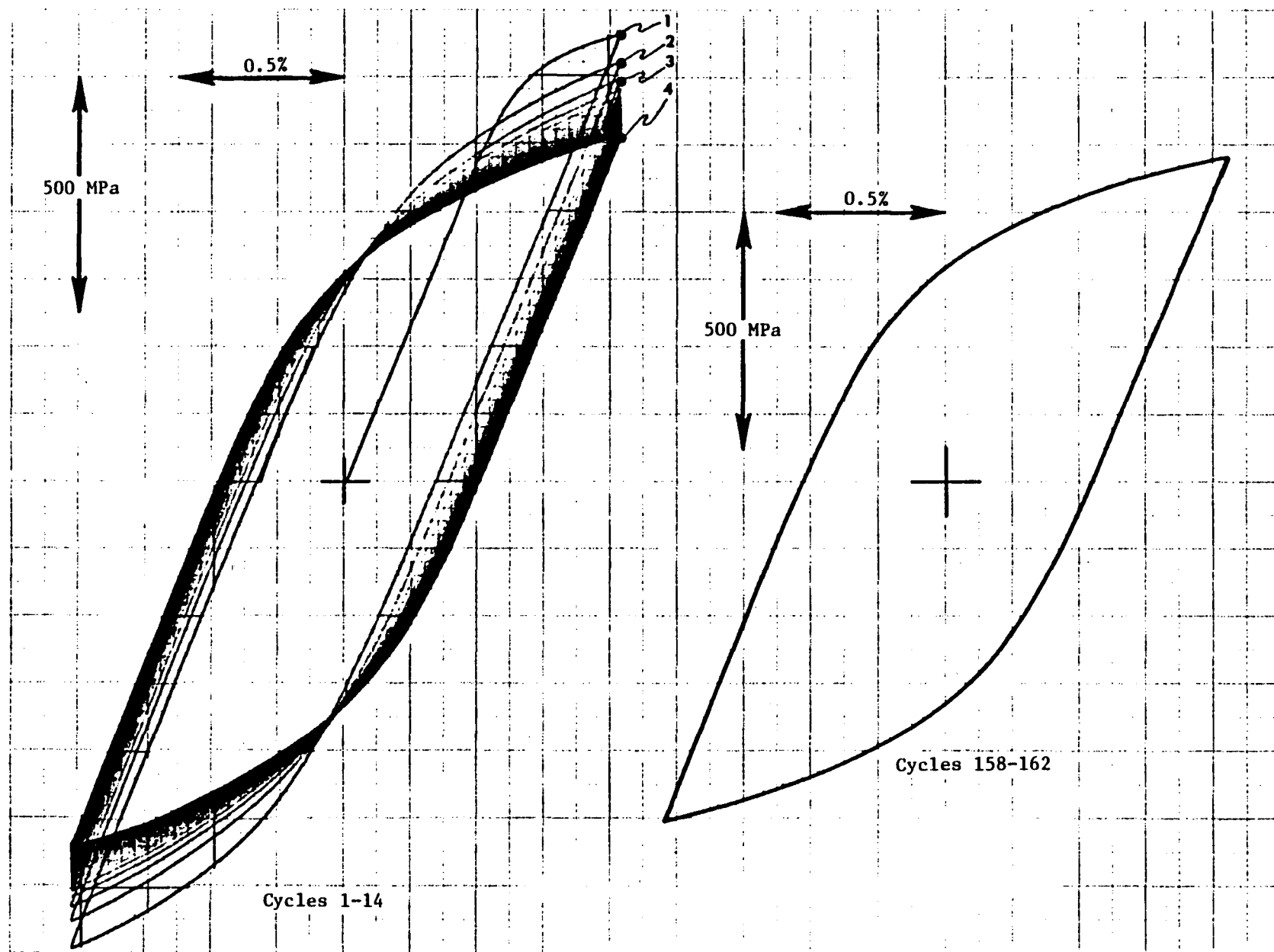


Figure 28. Examples of Alloy Hysteresis Loops in Cyclic Test (1200°F , $A_{\epsilon} = \infty$, 0.017 Strain Range, 2.0×10^{-4} Strain Rate).

stress approached zero. Figure 29 also shows a continuing softening in the cyclic test, but the softening rate diminished with increased cycling. This softening behavior is typical of Alloy 718 (Reference 19).

These results strongly suggest that the SEN specimen with a gage length of 15.9 mm (Figure 26) can be used as the primary specimen in this program. Additional tests are currently in progress to find the strain ranges where buckling occurs for positive and negative mean strains.

Another consideration in specimen design is the ASTM-recommended practice for the monotonic J-test requiring that the remaining uncracked ligament be smaller than $25 J/\sigma_y$ where σ_y is yield strength. It is recognized that for primarily tension cases, such as the SEN specimen, this criterion may be a poor estimate. Since it is planned to conduct tests for crack lengths ranging from 0.02 to 0.15 inch, calculations were performed to evaluate J, crack mouth opening displacement (δ), and crack tip opening displacement (δ_t) using the GE/EPRI Plastic Fracture Handbook (Reference 13). The 1200° F cyclic stress-strain curve for Alloy 718 was determined from the data in the NASA Benchmark Program (NASA CR-165571). Using this information, the parameters δ , δ_t , and J, along with \sqrt{EJ} (pseudo-K), were calculated for three values of crack length (0.05, 0.10, and 0.15 inch) and strain range (0.8, 1.6, and 2.4%). It was assumed for zero mean strain cycling ($R_\epsilon = -1$) that the crack was open only at positive loads, so the values of J, δ , and δ_t were calculated using the alternating stress range. The calculations were performed for both plane stress and plane strain conditions. The results of these calculations are summarized in Table VI. For the most severe case shown in Table VI, (0.15 inch crack length and strain range of 2.4%), the ASTM criteria are exceeded by factors of 6.4 and 3.3 for plane strain and plane stress conditions respectively.

For cyclic testing conditions, it may be more appropriate that the "process zone size" be smaller than the specimen thickness and remaining ligament. It is generally accepted that the process zone size is on the same order as δ_t . The most severe case listed in Table VI was δ_t values of less than 0.0005 inch. The specimen thickness and remaining ligament are 200 and 500 times larger than δ_t . On this basis, it is anticipated that this SEN can be used to select and evaluate P-I integrals under elastic-plastic conditions.

4.4.2 Displacement Control and Measurement

All SEN tests will be performed in a strain control mode with the experimental setup shown schematically in Figure 30. The controlling extensometer will be mounted at the center of the 10.2 mm wide surface of the specimen. Two other displacement gages, one to monitor crack mouth opening displacement (CMOD) and one to monitor the displacement on the face opposite the crack mouth, will also be used. The purpose of the CMOD gage is to detect when crack closure occurs. A standard 0.5 inch elevated temperature extensometer has been modified to have a gage length of approximately 0.03 inch and significantly improved resolution.

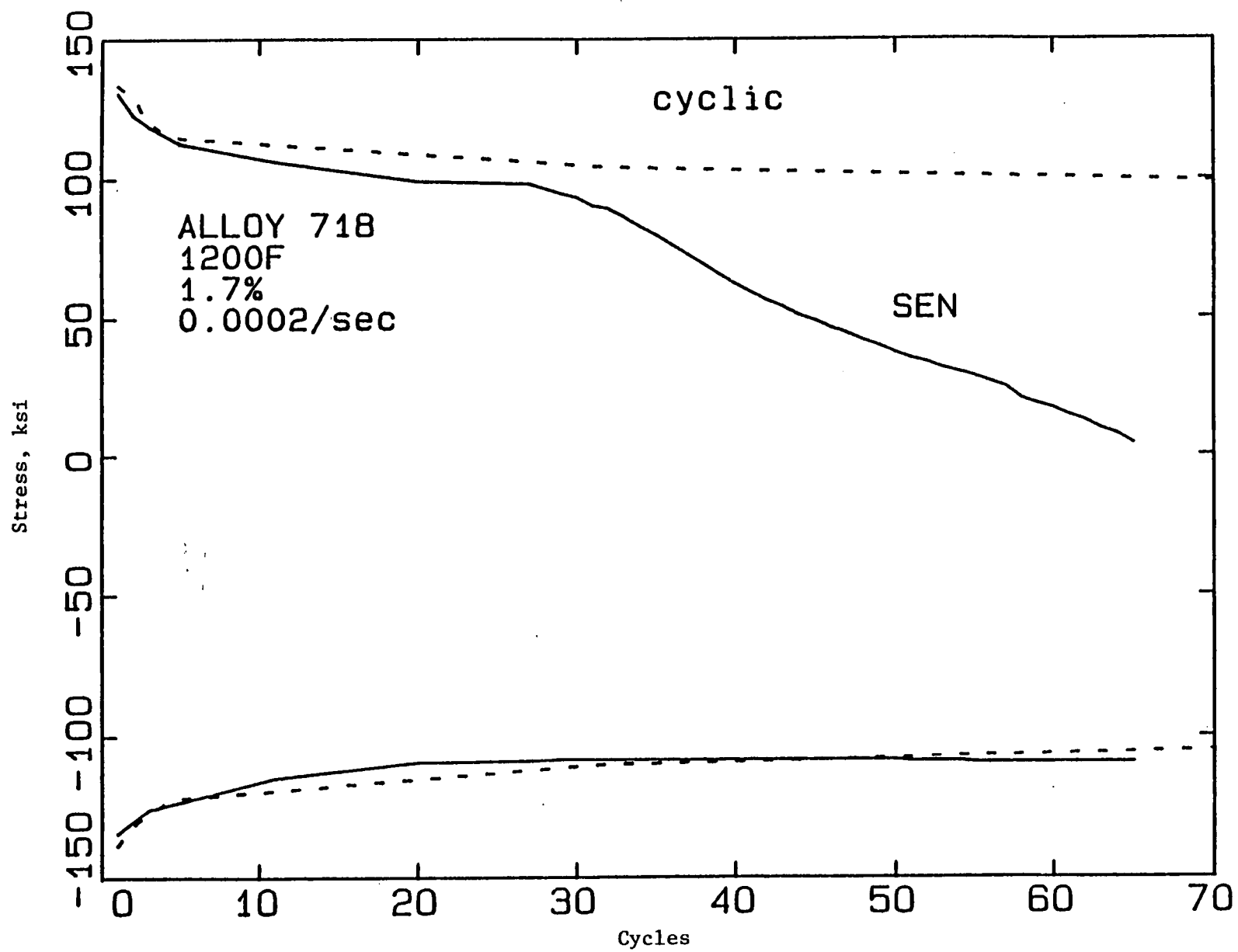


Figure 29. Variation of Maximum and Minimum Stress in Alloy 718 SEN and Cyclic Test.

Table VI. Summary of Estimated Values of J, δ , and δ_t for Alloy 718 at 1200° F.

Strain Range	Crack Length (in.)	Plane Stress				Plane Strain			
		J (ksi-in.)	\sqrt{EJ} (ksi $\sqrt{\text{in.}}$)	δ (in.)	δ_t (in.)	J (ksi-in.)	\sqrt{EJ} (ksi $\sqrt{\text{in.}}$)	δ (in.)	δ_t (in.)
.008	0.05	0.0111	16.3	0.000090	0.000025	0.0066	12.6	0.000056	0.000019
	0.10	0.0192	21.4	0.000285	0.000042	0.0109	16.1	0.000159	0.000032
	0.15	0.0433	32.2	0.000826	0.000091	0.0228	23.3	0.000439	0.000066
.016	0.05	0.0307	27.1	0.000180	0.000068	0.0183	20.9	0.000113	0.000053
	0.10	0.0530	35.6	0.000570	0.000118	0.0301	26.8	0.000317	0.000085
	0.15	0.1200	53.6	0.001651	0.000252	0.0630	38.8	0.000818	0.000183
0.24	0.05	0.0557	36.5	0.000270	0.000124	0.0333	28.2	0.000169	0.000097
	0.10	0.0962	47.9	0.000855	0.000213	0.0546	36.1	0.000476	0.000158
	0.15	0.2175	72.1	0.002474	0.000457	0.1143	52.3	0.001315	0.000332

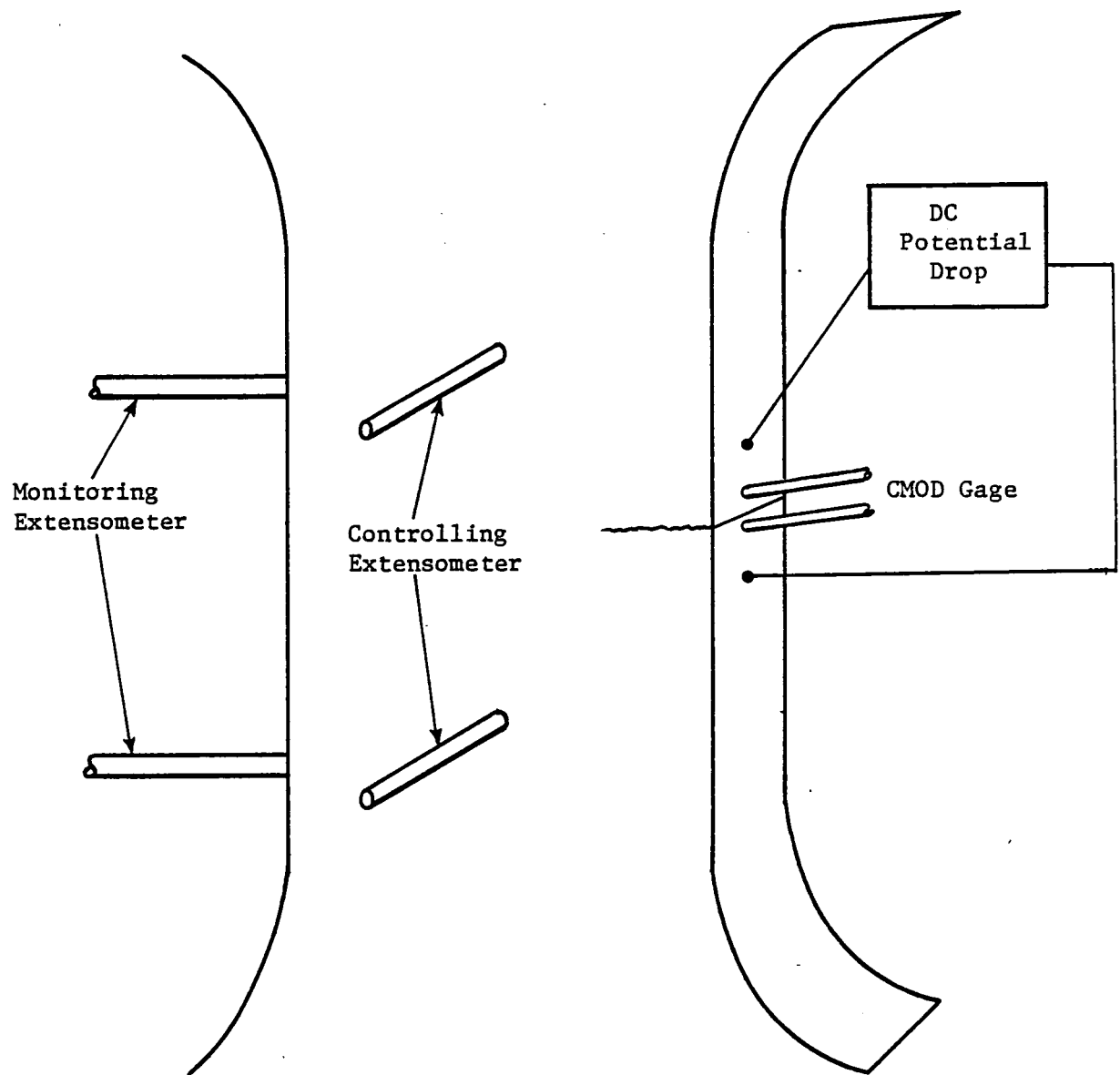


Figure 30. Schematic Drawing of SEN Test Method.

The stability of this prototype extensometer has been successfully evaluated at room temperature. It has also been demonstrated that the extensometer can be calibrated using a differential micrometer with a sensitivity of 0.0003 inch/volt which will give sufficient resolution for the subsequent experimental activities. The CMOD gage also measures the same value of strain measured with a conventional extensometer in an uncracked SEN specimen. The purpose of the monitoring extensometer is to furnish additional displacement information for setting the finite-element boundary conditions for verifying those results. The crack growth will be monitored using a direct current potential drop technique used extensively in linear elastic fracture mechanics characterization of materials with a pin-loaded SEN specimen (References 17 and 18). An ETS test control and data acquisition system (Reference 16) has been modified to monitor five channels and to provide a cycle pulse to trigger a direct current potential drop system with current switching.

All experimental apparatus is in place. The performance of each component has been verified separately. Work is in progress to integrate the entire test system. The alternate crack growth specimen will be a modified compact specimen (CT). The exact CT configuration and control mode have not been selected because of the difficulty in strain control and compressive loading of a CT specimen.

4.4.3 Test Plan

Table VII lists the proposed isothermal and TMF crack propagation test matrix. Duplicate test will be performed for each condition listed in Table VII. The strain ranges selected for the crack propagation tests are 0.5%, 1.15%, and 1.7%. The higher two ranges are also being used in the cyclic constitutive evaluation; at 1000° F, they correspond to plastic strain ranges of approximately 0.2% and 0.7% respectively. The 0.5% strain range should result in nominally elastic cycling.

A SEN specimen was also instrumented with multiple thermocouples to assess the uniformity of temperature during isothermal and TMF conditions. An RF (radio frequency) induction coil was designed to heat the entire gage length to isothermal conditions within 5° F. It has been shown that by simply turning the RF generator on and off, the coil design heats and cools the gage section over a temperature range of 800° to 1200° F. The temperature variation with time is almost linear and requires approximately 30 seconds to change the temperature by 400° F. Based on this result, the temperature ramp time will be controlled to be no smaller than 45 seconds so that the cyclic period will be greater than 90 seconds.

One of the considerations in this testing program is whether to conduct crack propagation tests under strain rate or under frequency control. Table VIII shows the cycle period and rate of cycle accumulation as a function of strain rate and strain range. For strain range conditions to be used in this program, the cycle period can vary by a factor of 3.4. This variation might induce some adverse environmental time-dependent crack growth components,

Table VII. Task VII Test Matrix.

	Specimen Geometry	Temperature, ° F	Strain Range	A_{ε}
Isothermal Crack Propagation	{ SEN	{ 800 1000 1000 1000 1100 1200 }	{0.005}	{ 1.0 ∞ -3.0 }
			{0.0115}	{ ∞ }
			{0.017}	
			{*}	{ ∞ }
TMF Crack Propagation	{ SEN	{ 800-1200 800-1000 }	{0.005}	{ ∞ , In Phase }
			{0.0115}	
			{0.017}	{ ∞ , Out Phase }
	{ CT	{ 800-1200 }	{*}	{ ∞ , In Phase ∞ , Out Phase }

* 2 Values, to be determined.

particularly at the more elevated temperatures (Reference 20). The initial cyclic tests suggest that Alloy 718 shows little strain rate sensitivity in cyclic constitutive response. Therefore, it is currently planned to conduct all crack propagation tests with 100-second cycles (864 cycles/day or 0.01 Hz).

Table VIII. Variation of Cycle Period and Cycle Accumulation in Strain Rate Controlled Tests With Strain Rate and Range.

$\dot{\epsilon}$ (sec ⁻¹)	$\Delta\epsilon$	Cycle Period, sec	Cycles/day
2×10^{-4}	0.005	50	1,728
	0.0115	115	751
	0.017	170	508
5×10^{-3}	0.005	2	43,200
	0.0115	4.6	18,783
	0.017	6.8	12,706

The TMF tests will be run with two temperature ranges: 800° to 1200° F and 800° to 1000° F. The temperature-time profile will have a triangular wave shape. The mechanical strain will have a similar profile. The thermo-mechanical cycling will be performed with both in-phase (maximum strain at maximum temperature) and out-of-phase (maximum strain at minimum temperature) cycling. The TMF tests will be performed in a computer-controlled TMF test facility at the General Electric EMTL Testing Laboratory (Reference 21).

4.5 TASK VIII - CRACK PROPAGATION WITH THERMAL GRADIENT, ANALOG MATERIAL

A total of eight SEN specimens will be tested with a thermal gradient across the gage section to verify that the path-independent integral can predict crack growth under this condition. It is planned to run a gradient from 800° F to 1200° F across the 0.4-inch dimension of a SEN specimen. Duplicate tests will be performed under monotonic loading with alternating strain ranges of 0.005, 0.0115, and 0.017 with A_{ϵ} of ∞ .

5.0 COMPUTER SIMULATION OF SEN SPECIMENS

Computational analyses and experimental measurements under the present work are directed toward single-edge-notched (SEN) specimens containing edge cracks subjected to displacement control loading conditions. As such, the bulk of the computer simulation effort is focused on numerical analysis of the SEN specimens. The analytical results obtained are then compared with the experimental data generated in the present program. A buttonhead geometry was selected to facilitate tension and compression loading of the SEN specimens.

To simulate the prescribed displacement boundary conditions for two-dimensional (2D) analysis of the gage section of the buttonhead SEN specimen, three-dimensional (3D) finite-element analysis was performed for the entire buttonhead specimen. Figures 31 and 32 show the 3D mesh of the buttonhead specimen consisting of eight-noded isoparametric brick elements. The model has 1107 nodes and 720 elements. It has considerable mesh refinement along the length of the specimen in order to accurately predict stresses and displacements along the axial direction for the purpose of extracting boundary conditions for subsequent 2D analysis of the gage section. The ratio of gage section length to width (L/W) is 1.125, and the single-edge crack-length-to-width ratio (A/W) is kept at 0.25. This crack length represents an upper bound for the maximum A/W ratio to be analyzed in the program.

Elastic analysis was completed for two different cases of applying prescribed end-displacements to the model. In one case a constant axial displacement was applied to the buttonhead, while in the second case the constant displacement was applied on the top portion of the specimen shank circumference adjacent to the buttonhead. These two boundary conditions were used to simulate the uncertainty in the actual displacements induced by the laboratory gripping fixtures. By equating the resulting elastic axial displacement (U_y) at a given node-point in the gage section of the model, it was found that the two end-displacement cases have a maximum of 3% difference in stresses and displacements across the width of the gage section. Therefore, it is concluded that for elastic response, the application of constant end displacement to either the buttonhead or the shank-top leads to almost identical results in the gage section. Figure 33 shows the completed elastic axial displacement (U_y) along the gage section width for different axial cross sections (Y/L ratios). A constant axial displacement of 0.01 inch was applied at the shank-top in an Alloy 718 specimen at room temperature. It can be seen in Figure 33 that U_y displacement varies linearly along the gage section width for the top half of the gage length. This linear variation will make it easier to make displacement measurements using just two extensometers.

Elastic axial stress (σ_{yy}) response across the gage section width is shown in Figure 34. In the absence of a crack, uniform σ_{yy} normal stress is 366 ksi in the gage section. Due to the presence of a crack ($A/W = 0.25$), the maximum normal stress concentration factor at the crack plane ($Y/L = 0$) is 1.72, which reflects the fact that the crack-tip singularity is symbolic at best in the present mesh refinement at the crack plane. The σ_{yy} normal stress

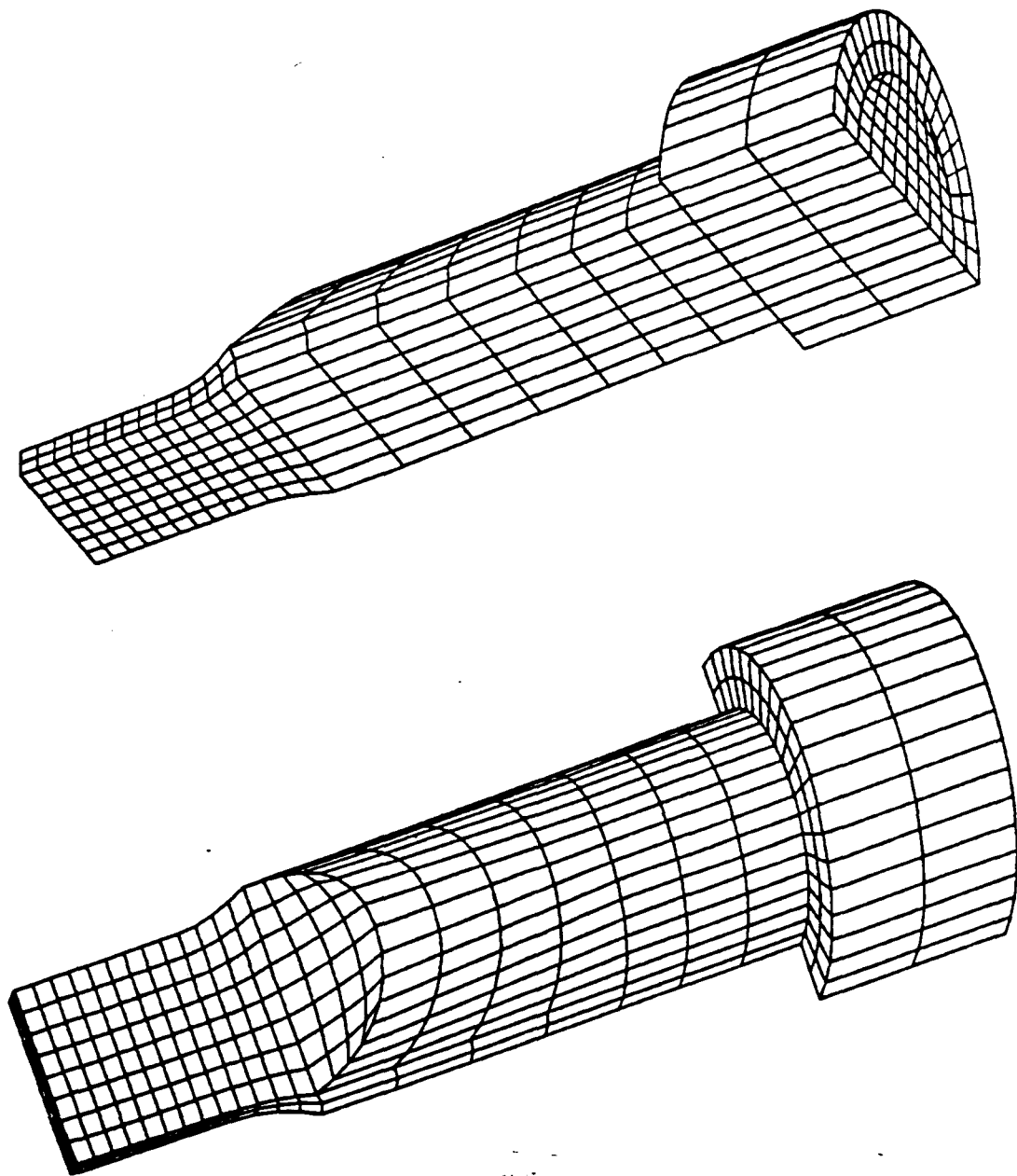


Figure 31. Buttonhead Specimen Three-Dimensional Finite-Element Model.

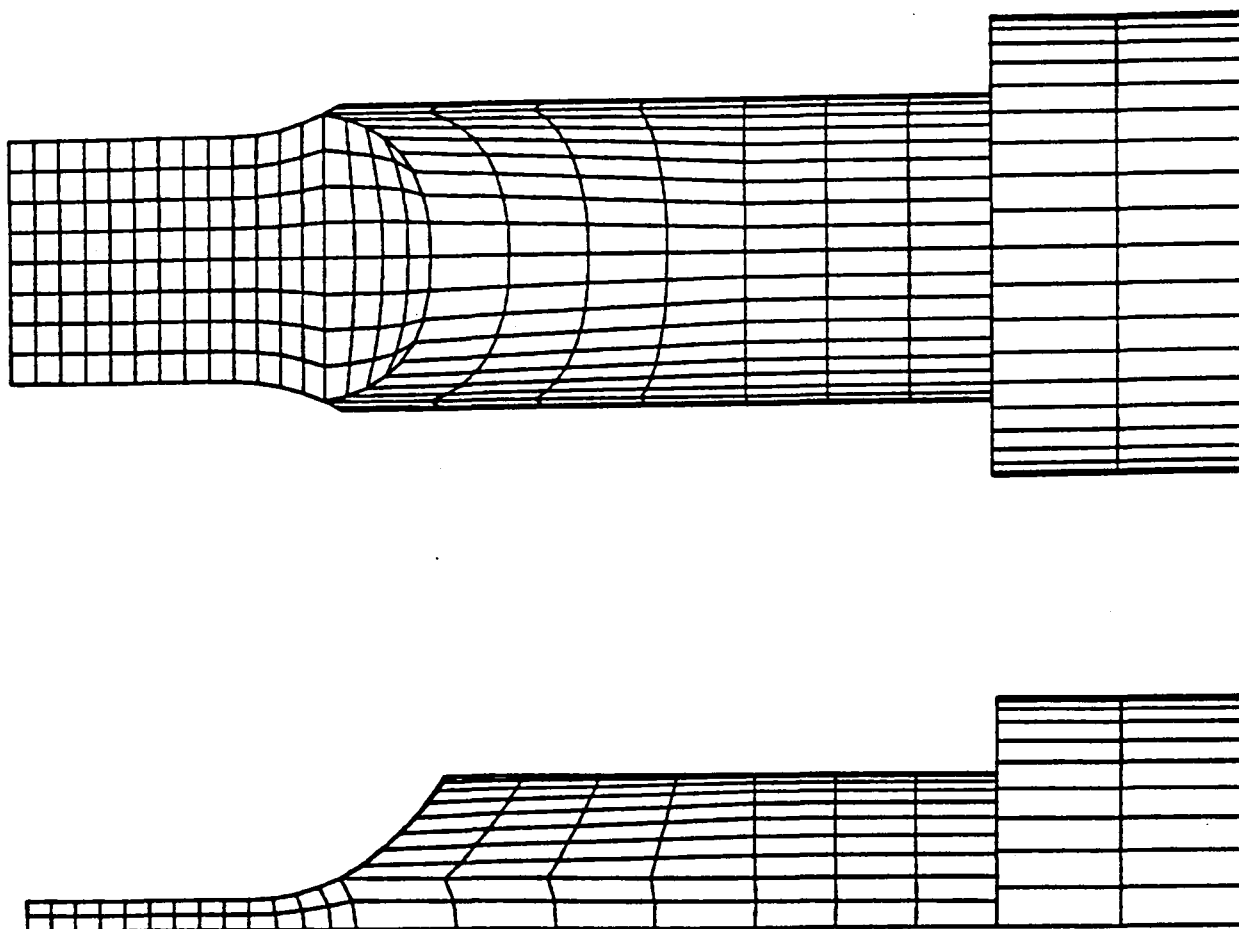


Figure 32. Top View and Elevation of the SEN Buttonhead Specimen Three-Dimensional Finite-Element Model.

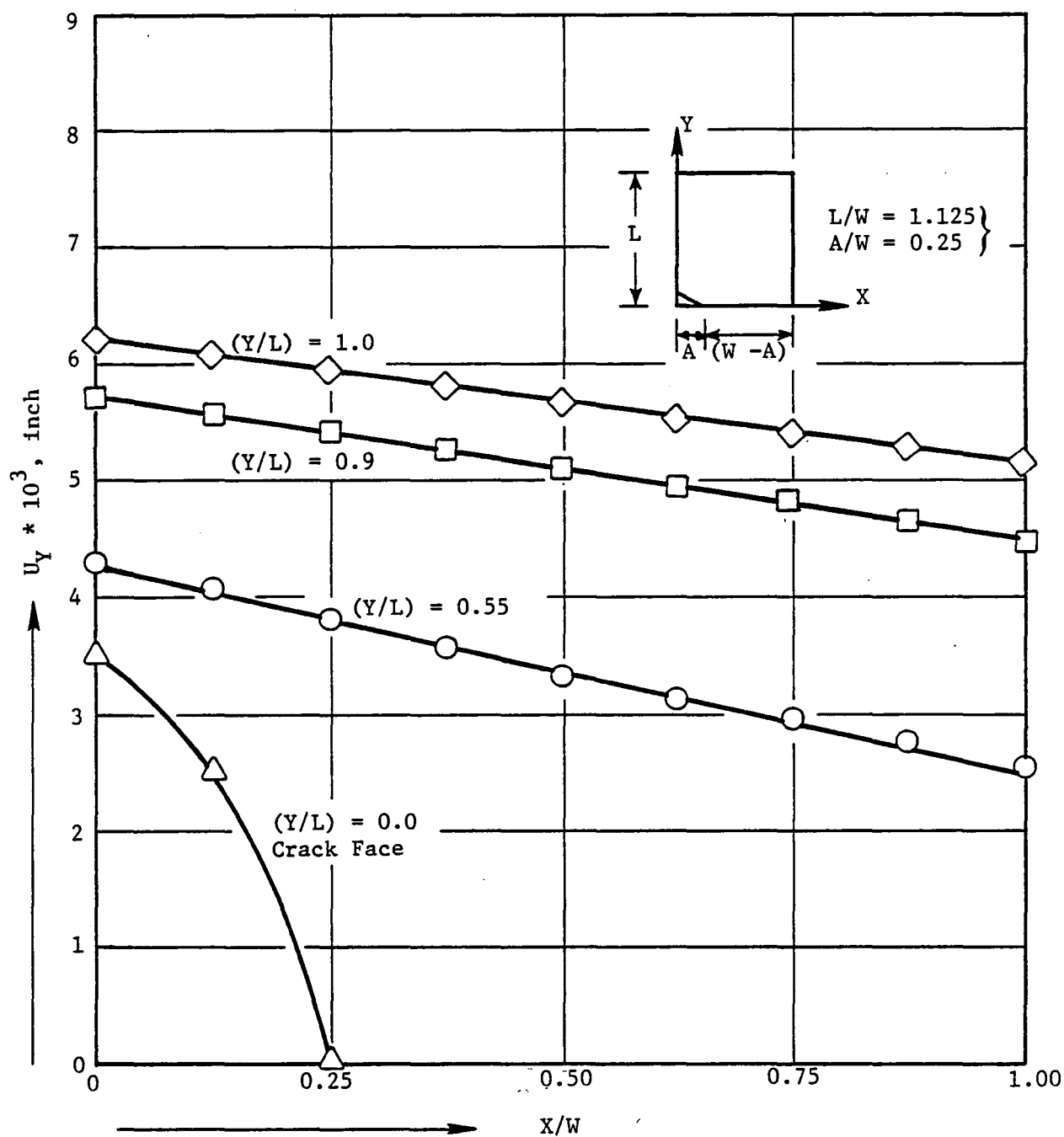


Figure 33. Normal Displacement Variation in Gage Section for Three-Dimensional Elastic Analysis of Specimen Subjected to Constant Axial Displacement at Buttonhead.

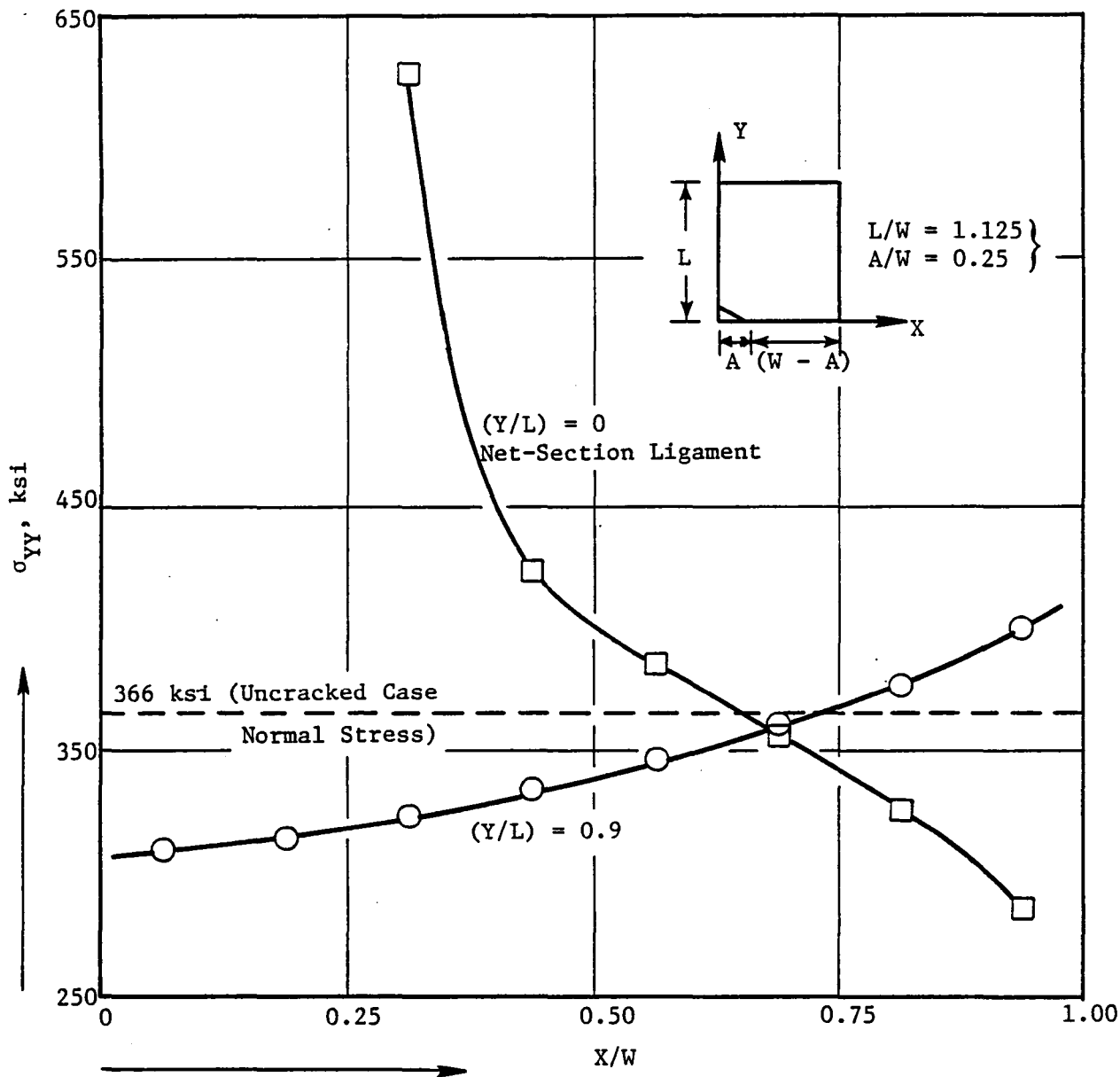


Figure 34. Normal Stress Variation in Gage Section for Three-Dimensional Elastic Analysis of Specimen Subjected to Constant Axial Displacement at Buttonhead.

variation at a cross section near the top of the gage length ($Y/L = 0.9$) shows an interesting feature of the bending stress component along the width of the specimen. Because of parabolic variation of the σ_{yy} normal stress at $Y/L = 0.9$ cross section, it is inferred that the bending component of normal stress increases as one moves across the gage section width from the crack mouth ($X/W = 0$) to the back surface ($X/W = 1$).

From these results, it is concluded that for elastic 2D simulations of the gage section in buttonhead specimens subjected to prescribed constant axial displacement, one needs to impose a linearly varying normal displacement (shown in Figure 33) at the top cross section ($Y = L$) of the gage length.

Figure 35 shows the deformed shape of the SEN crack specimen subjected to a uniform 0.01-inch axial tensile displacement of the buttonhead. It can be seen that the specimen lateral displacement in the crack plane is of the same order (0.0035 inch) as the crack-mouth opening displacement (CMOD). This is because the buttonhead is fixed against lateral movement, and the bending moment due to the presence of crack causes the specimen to deform laterally in the crack plane where it has the lowest stiffness.

Additional work is continuing on elastoplastic finite-element analysis of the buttonhead SEN specimen 3D model to extract boundary conditions for an equivalent 2D representation of the specimen gage section for inelastic analyses. Work is also continuing on a 2D finite-element model with gap elements to simulate the effects of reversed loading and the resulting crack closure on various P-I integrals.

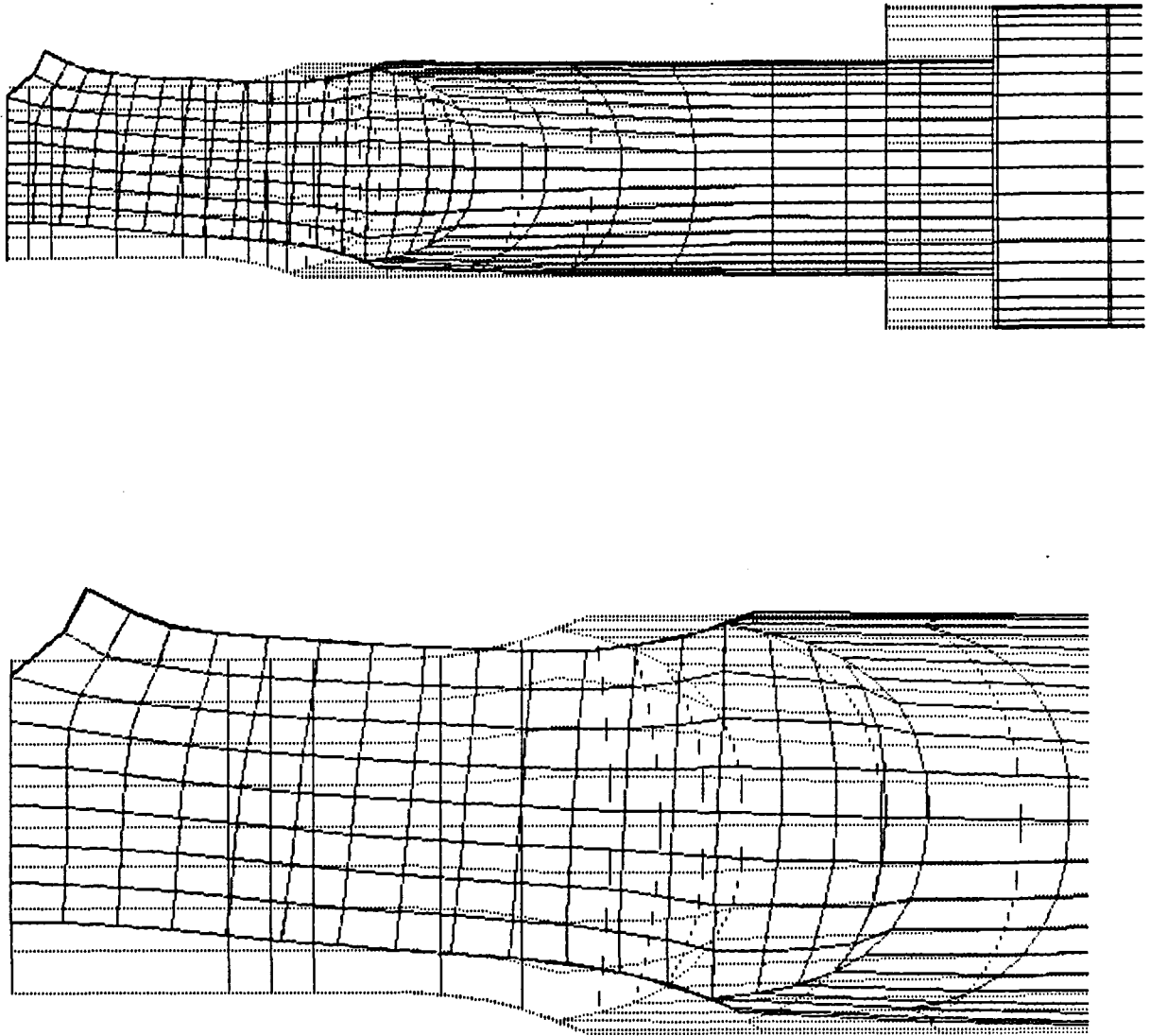


Figure 35. Lateral Displacement Profile of the Buttonhead Single Edge Crack Specimen Subjected to Uniform Axial Displacement (Dotted Lines Show Undeformed Shape).

6.0 DISCUSSION

This report has documented activities of the first year of the NASA-sponsored Elevated Temperature Crack Growth Program. As shown in the report, excellent progress has been made in all phases of work.

The review in Section 2.0 of path-independent (P-I) integrals considered several important requirements for gas turbine applications at elevated temperatures and selected the most promising ones for further work. The discussion in Section 2.0 is brief because the full review was documented in detail in Reference 1.

Section 3.0 discusses the successful development of a finite-element postprocessor computer program to calculate P-I integrals. This work shows the tendencies of proposed parameters that will be evaluated in future experimental work on this program.

Section 4.0 describes the experimental work and material selection activities. During the past year, a single-edge-notch (SEN) specimen was designed and verified for use in this program. This SEN specimen is capable of fully reversed loadings in the inelastic strain region and can be tested in thermo-mechanical fatigue. A crack-mouth opening displacement (CMOD) measurement device with a 0.76-mm gage length was developed for use with the SEN specimen. Alloy 718 was selected as the analog material, and initial smooth-specimen testing was conducted on this material.

In Section 5.0, the results of three-dimensional finite-element analyses were presented. These analyses are being conducted to establish the appropriate boundary conditions for the two-dimensional work to be performed during 1985.

7.0 REFERENCES

1. Kim, K.S., "A Review of Path-Independent Integrals in Elastic-Plastic Fracture Mechanics," Annual Contractor Report, NASA Lewis, LR-174956, 1985. Also presented in ASTM 18th National Symposium in Fracture Mechanics, June 1985.
2. Rice, J.R., "A Path-Independent Integral and the Approximate Analysis of Strain Concentration by Notches and Cracks," Journal of Applied Mechanics, Vol. 35, 1968, pp. 379-386.
3. Wilson, W.K., and Yu, I.W., "The Use of the J-Integral in Thermal Stress Crack Problems," International Journal of Fracture, Vol. 15, 1979, pp. 377-387.
4. Gurtin, M.E., "On a Path-Independent Integral for Thermoelasticity," International Journal of Fracture, Vol. 15, 1979, pp. R169-R170.
5. Ainsworth, R.A., Neale, B.K., and Price, R.H., "Fracture Behavior in the Presence of Thermal Strains," Proceedings of Institute of Mechanical Engineers' Conference on Tolerance of Flaws in Pressurized Components, London, 1978, pp. 171-178.
6. Blackburn, W.S., "Path-Independent Integrals to Predict Onset of Crack Instability in An Elastic Material," International Journal of Fracture Mechanics, Vol. 8, 1972, pp. 343-346.
7. Blackburn, W.S., Jackson, A.D., and Hellen, T.K., "An Integral Associated with the State of a Crack Tip in a Nonelastic Material," Vol. 13, 1977, pp. 183-200.
8. Kishimoto, K., Aoki, S., and Sakata, M., "On the Path-Independent Integral-J," Engineering Fracture Mechanics, Vol. 13, 1980, pp. 841-850.
9. Atluri, S.N., Nishioka, T., and Nakagaki, M., "Incremental Path-Independent Integrals in Inelastic and Dynamic Fracture Mechanics," Georgia Institute of Technology Report No. GIT-CACM-SNA-83-27, May 1983; Also in Engineering Fracture Mechanics, Vol. 20, 1984, pp. 209-254.
10. Miyamoto, H., and Kageyama, K., "Estimation of the J-Integral to the General Elastoplastic Problem and Suggestion of a New Method for its Evaluation," Proceedings of the First International Conference on Numerical Methods in Fracture Mechanics, Swansea (Wales), ed. A.R. Luxmoore and D.R.J. Owen, 1978, pp. 479-486.
11. Miyamoto, H., and Kikuchi, M., "Evaluation of the Three-Dimensional J-Integral of the CT Specimen in Elastoplastic States," Transactions of Sixth International Conference on SMIRT (Structural Mechanics in Reactor Technology), Vol. 1, 1981, Paper L6/4.

REFERENCES (Concluded)

12. Kikuchi, M., and Miyamoto, H., "The Thickness Effect of Side-Grooved CT Specimens," International Journal of Pressure Vessel and Piping, Vol. 16, 1984, pp. 1-16.
13. Kumar, V., German, M.D., and Shih, C.F., "An Engineering Approach for Elastoplastic Fracture Analysis," EPRI Report NP-1931, Research Project 1237-1, Electric Power Research Institute, Palo Alto, CA, July 1981.
14. Nakagaki, M., and Atluri, S.N., "On a Study of the (\dot{T}) Integral in Fracture Analysis of Solids With Inelastic Rate Constitutive Laws," ASME Journal of Pressure Vessel Technology, Vol. 104, 1982, pp. 331-337, and Vol. 105, 1983, p. 79.
15. Nakagaki, M., Atluri, S.N., and Nishioka, T., "On the Path-Independent Integral, ΔT_p , in Elastic-Plastic Fracture Mechanics," Proceedings of SECTAM-XII Conference, Pine Mountain, GA, May 1984.
16. Ramaswamy, V.G., Van Stone, R.H., Dame, L.T., and Laflen, J.H., "Constitutive Modeling for Isotropic Materials," Annual Contractor Report, NASA Lewis, CR-17485, October 1984.
17. Van Stone, R.H. and Krueger, D.D., "Investigation of Direct Aged Inconel 718 Fatigue Behavior," Contract N00019-82-C-0373, Final Report, December 1984, General Electric Co., Cincinnati, Ohio 45215.
18. Jang, H., Wright, P.K., "Fatigue and Fracture of Advanced Blade Material," Air Force Wright Aeronautical Laboratories, Report TR-84-4166, February 1985.
19. Cook, T.S., ASTM STP 765, ASTM, Philadelphia, PA, 1982, pp. 269-283.
20. Coles, A., Johnson, R.F., and Popp, H.G., Journal of Eng. Matl. Tech., Volume 98, 1976, p. 305.

1. Report No. CR-174957		2. Government Accession No.		3. Recipient's Catalog No.	
4. Title and Subtitle ELEVATED TEMPERATURE CRACK GROWTH				5. Report Date August 1985	
				6. Performing Organization Code	
7. Author(s) J.F. Yau, S.N. Malik, K.S. Kim, R.H. Van Stone, and J.H. Laflen				8. Performing Organization Report No.	
9. Performing Organization Name and Address General Electric Aircraft Engine Business Group Advanced Technology Programs Department Cincinnati, OH 45215				10. Work Unit No.	
				11. Contract or Grant No. NAS3-23940	
12. Sponsoring Agency Name and Address National Aeronautics and Space Administration Washington, DC 20546				13. Type of Report and Period Covered First Annual Status Report	
				14. Sponsoring Agency Code	
15. Supplementary Notes Project Manager, T.W. Orange NASA Lewis Research Center (MS 49-6) 2100 Brookpark Road Cleveland, OH 44135					
16. Abstract The objective of the Elevated Temperature Crack Growth Project is to evaluate proposed nonlinear fracture mechanics methods for application to combustor liners of aircraft gas turbine engines. During the first year of this program, proposed path-independent (P-I) integrals were reviewed for such applications. Several P-I integrals were implemented into a finite-element postprocessor which was developed and verified as part of the work. Alloy 718 was selected as the analog material for use in the forthcoming experimental work. A buttonhead, single-edge notch specimen was designed and verified for use in elevated-temperature strain control testing with significant inelastic strains. A crack mouth opening displacement measurement device was developed for further use.					
17. Key Words (Suggested by Author(s)) Nonlinear Fracture Mechanics Finite-Element Analysis Path-Independent Integrals Crack Mouth Opening Displacement Thermal Gradients Thermal/Mechanical Fatigue				18. Distribution Statement Unclassified, Unlimited	
19. Security Classif. (of this report) Unclassified		20. Security Classif. (of this page) Unclassified		21. No. of Pages : 22. Price* 63	

* For sale by the National Technical Information Service, Springfield, Virginia 22161

End of Document